To the University of Wyoming:

The members of the Committee approve the thesis of Troy E. Lake, Jr. presented on 28 April 2017.

Dr. Dimitri Mavriplis, Chairperson

Dr. Craig Douglas, External Department Member

Dr. Michael Stoellinger

Dr. Brian Allan

APPROVED:

Dr. Carl P. Frick, Head, Department of Mechanical Engineering

Dr. Michael Pishko, Dean, College of Engineering and Applied Science

Lake, Jr., Troy E., Adjoint based, Error Controlled, Loosely Coupled, Unstructured Design Optimization and Adaptive Mesh Refinement Using FUN3D, M.S., Department of Mechanical Engineering, May, 2017.

Adjoint-based design problems are dependent on the sensitivities from the CFD solution. Current best practices for these adjoint based design problems use fixed-complexity computational meshes that are built using developed best practices. An issue with these fixed-complexity computational meshes is that flow features may not be properly or completely captured. To improve the accuracy of the solution and the sensitivities, the mesh can be adaptively refined to reduce the discretization error within the flow solution. By adapting the mesh, the size of the mesh may be reduced as well, increasing the computational efficiency of the design problem. The computational efficiency of the design problem may also be improved with the use of progressive design variable parameterization. This research focuses on developing methodologies for variations of current best practices methods for design optimization problems including the use of adaptive mesh refinement. The design optimization and mesh adaption processes utilize the built-in tools within FUN3D, linked to the SNOPT optimizer for geometry optimization. To justify the benefits of the coupled mesh adaptation and design optimization, the final value of the objective function, complexity of the computational mesh, and the Optimization Complexity Function for each case are used as comparison points. An inviscid, non-lifting airfoil, and a viscous, lifting airfoil are used as test cases for this research. The baseline case uses a fixed parameterization scheme, and comparison cases exploit progressive parameterization to aid in creating optimal shapes while avoiding the introduction of irregular shape features. Fixed complexity mesh optimization cases are compared with loosely coupled adaptive mesh refinement (AMR) and optimization cases. The family of fixed-complexity meshes are also used in a progressive mesh complexity method, starting with the coarse mesh and then transitioning the final design to the next finest mesh. During the research, it was found that the more design variables used during the optimization, the better the resulting optimal airfoil. For a 31 design-variable case, the final

drag was reduced by approximately 430 counts over the initial airfoil shape. The number of flow solver calls for optimization was found to increase with the number of design variables and with mesh complexity. Progressive parameterization was shown to reduce the number of flow solver calls for equivalent or superior design outcomes. AMR was shown to reduce the mesh complexity for the solution, but was not always cheaper, as there is an increase in user interaction with the coupled design optimization and mesh adaption process. The most efficient results from this research were the progressive mesh complexity approach combined with progressive parameterization. This method allowed for much more rapid objective function convergence on finest meshes and with refined parameterizations on the finest meshes that were previously deemed too computational expensive. Based on these findings, future work should investigate a progressive error tolerance study using adaptive mesh refinement for design optimization. Additionally, anisotropic mesh adaption should be considered for RANS cases, as isotropic adaption was shown to be impractical for the solution of viscous turbulent flows over airfoil configurations.

ADJOINT BASED, ERROR CONTROLLED, LOOSELY COUPLED, UNSTRUCTURED DESIGN OPTIMIZATION AND ADAPTIVE MESH REFINEMENT USING FUN3D

by

Troy E. Lake, Jr., B. S. A. E.

A thesis submitted to the
Department of Mechanical Engineering
and the
University of Wyoming
in partial fulfillment of the requirements
for the degree of

MASTER OF SCIENCE
in
MECAHNICAL ENGINEERING

Laramie, Wyoming
May 2017

To my family, both related and the friends that have become family. Without you, this would not have been possible.

Contents

List of Figures

List of Tables

Acknowledgments

I would like to acknowledge Dr. Dimitri Mavriplis for taking me on as a student, allowing me to come back home to Wyoming, and directing my research. My committee for taking their time to help with this research. My parents and brother for all the support they have provided for me. Dr. Brian Allan for his mentorship and help throughout the last two years. Dr. Michael Park for his assistance and guidance here at NASA Langley during my research phase. Catherine McGinley and Luther Jenkins for the opportunity to work here at NASA while finishing my research, and their patience. Dr. Marlyn Andino for sharing an office with me and being a sounding board about work and life during this time. Enrico Fabiano for all his help and friendship. Dr. Elizabeth Ward for being my NASA mom. Lindsey Carboneau and Michael Staab for their editing help and patience with my writing. Norma Farr, Dr. Douglas Nark, Michael Wiese, Carrie Rhoades, Thomas Britton, and the rest of the Afterburner group to remind me to relax and to not take yourself too seriously.

Troy E. Lake, Jr.

University of Wyoming

May 2017

Chapter 1

Introduction

1.1 Motivation

Design optimization offers a way to increase performance and efficiency requirements for aerospace vehicles. Design optimization varies parameters, e.g., camber or thickness, to minimize objective functions (the design goals) for each problem. These objective functions can include a desired sonic boom signature of the vehicle, lift, pitching moment, or drag value. High fidelity aerodynamic design optimization is a field within computational fluid dynamics, which takes continuous partial differential equations, e.g., the Navier-Stokes equations, discretizes them on a computational mesh, and then creates an optimal shape for a given set of requirements within a given flow field. The discretization process introduces unquantified discretization error into the solution, i.e., the difference between the solution of the continuous partial differential equation and that of the discretized partial differential equation. Traditional design optimization uses fixed computational meshes developed using common best practices and experience-gained knowledge. This method often provides optimal designs on a given computational mesh, but significant challenges may arise. If considerable geometric changes occur, significant discretization error may arise from the

emerging flow physics. To capture these new physics, a user may recreate the computational mesh to better capture the flow features of the more optimal shape. A highly refined initial computational mesh can also capture these emerging flow physics, though the associated computational expense may make this approach infeasible. An alternative approach controls the discretization error associated with emerging flow physics by loosely coupling the design optimization process with error estimators and mesh adaption. Consequently, the exact discrete sensitives calculated using the flow solution with reduced discretization errors results in a flow solution which follows the continuous partial differential equations more closely. This thesis focuses on finding optimal configurations for a desired objective function constrained to the discrete partial differential equations by controlling the discretization error with error estimation and mesh adaption. A comparison between recreating fixed-complexity computational meshes and the discretization-error-controlled computational meshes demonstrates the benefit of controlling the discretization error with error estimation and mesh adaption during the design optimization process. This comparison includes the optimization complexity function values, differences between the computed final objective functions, and output quantities, such as lift and drag.

Li and Hartmann [1] performed a similar comparison using the AIAA Aerodynamic Design Optimization Discussion Group (ADODG) [2] case 1. Li and Hartmann's research used a two-dimensional, inviscid, Discontinuous Galerkin finite-element method. The resulting design, using adaptive mesh refinement, proves more optimal than the design using the original computational mesh while maintaining the same number of degrees of freedom. In this test case from the ADODG, the shape changes dramatically, causing the shock to shift from a location of approximately two-thirds of the chord to the trailing edge of the airfoil. The shock transitions from a straight normal shock to a more curved shock, with the formation of a lambda shock not present on the initial shape. While able to provide improvement over the initial computational mesh, recreating computational meshes between

design optimization cycles does not ensure complete capture of the new features. Li and Hartmann demonstrated a more optimal design by incorporating adaptive mesh refinement in the design optimization process. Li and Hartmann also showed a decrease in required computational time to reach the more optimal solution.

Anderson et al. [3] performed a similar comparison of the ADODG case 1 using CART3D [4]. Anderson showed a decrease in number of design searches required to reach an optimal solution by using progressive parameterization. This comparison used adaptive mesh refinement and adaptive design-variable parameterization. Adaptive design-variable parameterization refers to the number of design variables and design-variable locations changing during the optimization process. The design-variable parameterization used both fixed and progressive parameterization.

By automating the computational mesh building process, adaptive mesh refinement reduces direct user interaction, requiring little a priori knowledge of the flow physics to reach a numerically accurate solution. Mesh adaption and grid error estimators only resolve required areas based on the flow physics, thus lowering the computational cost. The discretization-error-controlled adaptive mesh refinement technique presented targets objective function error and an additional grid-error term, as defined in reference [5].

The research presented in this thesis performs similar comparisons between the fixed-complexity computational meshes and a discretization-error-controlled adapted mesh described by Li and Hartmann [1], though with notable differences between the two applications. This research used one error tolerance level, like Anderson [3], while Li and Hartmann used multiple error tolerance levels. Li and Hartmann used a finite-element method with curved elements and this research used a finite-volume method with isotropic unstructured elements, a more common approach in the aerospace industry. Anderson used a finite-volume approach with Cartesian cut cells. Li and Hartmann also used element splitting mesh adaption whereas this research uses a metric-based adaption approach. Anderson used a cell

splitting method for adaption. The metric-based adaption allows for more user control of the adaption process and the use of anisotropic computational mesh cells, though these are not used for this research.

1.2 Literature Survey

Presented in the following subsections is a literature review covering design optimization coupled with adaptive mesh refinement and the individual components which make up the coupled process. This provides a general background to place the current research into context with previous research.

1.2.1 Design Optimization

Design optimization covers many different approaches and methodologies. Therefore, only sources which highlight the techniques utilized in this research are documented. Jameson [6] provided a brief history of design optimization over the past 30 years, centered around transonic flow conditions. Jameson discussed the importance of understanding this regime, and then subsequently demonstrated [7] this with an Euler code for both 2D and 3D design optimization, as well as provided information on adjoint formulations. The results demonstrate the difficulties of transonic design and that even "optimal" solutions can be improved. A set of lectures by Vassberg and Jameson given at the Von Karman Institute [8, 9] discussed approaches to design optimization problems, as well as background on the importance of optimization. Lecture 1 [8] introduced theoretical background on commonly used techniques for aerodynamic design optimization and application of these techniques to simple problems, i.e., The Spider and The Fly. Lecture 2 [9] extended the application of the techniques presented in Lecture 1 [8] to both industry and research. Mavriplis [10] demonstrated the implementation of the discrete adjoint for three-dimensional optimization

problems on unstructured meshes. The adjoint formulation is compared to the forward sensitivity formulation on a transonic aircraft with a weighted penalized objective function. This comparison demonstrated a tangent used to verify the adjoint, concluded with a time savings seen by the adjoint formulation once a larger number of design variables are manipulated during optimization. To improve aerospace design techniques, Poole [11] identified two global search algorithm methods - partial swarm and gravitational search algorithms - as potentially useful for aerodynamic problems, and developed a global search algorithm framework based on this. Poole [12] discussed and compared adjoint-based optimization schemes and the global search algorithm framework for subsonic, two-dimensional flow conditions. Poole concluded that the global search algorithms can reduce the drag further than adjoint methods in most cases, though at a substantial increase in computational cost. This increase in computational cost for global search methods indicates adjoint methods will continue in design optimization cases moving forward as improvements in computational costs to global search methods are made. Buckley [13] utilized real-world requirements to perform airfoil optimizations with penalty-method objective functions. These requirements included off-design situations, as aircraft are not always in the on-designed situation. To meet these off-design requirements, the weights within the penalty function were surveyed, allowing for an alternative to computation of multiple adjoints. This alternative is useful for the coupled process of design optimization and adaptive mesh refinement, as there remains a significant amount of research on how best to implement multiple adjoints for adaptive mesh refinement.

1.2.2 Shape Parameterization Methods

The parameterization of an optimization problem greatly influences the final shape. Depending on the limitations placed on the parametrization, the resulting final shape may move between local minima without ever approaching the global minimum for the target function. Additionally, the type of parameterization impacts the final shape, as certain features may

or may not be attainable depending on the form of parameterization. Samareh [14] surveyed shape parameterization methods, comparing each over a set of features, such as what is parameterized, i.e., the computational mesh or the surface, whether for a structured or unstructured mesh, and how the shape is perturbed. Samareh stressed that the choice of shape parameterization method depends on the problem specific requirements, noting that aerospace design optimization problems include the entire aerospace vehicle, not just the aerodynamics. The third lecture by Vassberg and Jameson [15] also surveyed the impact of the shape parameterization method on the final optimized solution. Vassberg and Jameson provided viscous and inviscid design optimization cases, comparing the results of the final shape but emphasizing that there is no global optimal shape parameterization method. Samareh [16] detailed the creation and structure of MASSOUD, the parameterization tool used in this research. MASSOUD parametrizes a perturbation plane rather than the geometry itself using aerodynamic terms such and camber and thickness. This method allows for a more natural approach to design optimization, as the user can better visualize what is being perturbed more rapidly. This allows for easier user constraints for aerodynamic problems, such as thickness or twist, for more realistic geometry creation. Castonguay [17] surveyed the impact of the shape parameterization method on the final shape for a two-dimensional inverse design case and a drag minimization case. The shape parameterization methods were ranked per the accuracy of the inverse design and resulting objective function value for drag minimization. Mousavi [18] extended this survey to three-dimensions, performing the same ranking as Castonguay [17]. Anderson [19] surveyed techniques for deforming surfaces and details the creation of a new tool which utilizes Blender [20], an open source three-dimensional modeling tool used by the animation community. By employing Blender, Anderson utilized the advanced geometry definition and manipulation techniques developed by the digital animation industry. The fixed parameterization work by Anderson extended to an adaptive shape parameterization method [21]. This adaptive shape parameterization

method allowed for design variables to be adjusted on the surface for better utilization of computational resources during design optimization problems, similar to the use of adaptive mesh refinement for computational meshes.

1.2.3 Adaptive Mesh Refinement

The final individual component used in this work consists of the adaptive mesh refinement strategy. Multiple approaches may be taken to adapt a mesh; therefore, only the techniques which are applicable to this research are covered. Park [22] surveyed current adaptive mesh refinement research and outlined suggestions for research areas in the future, particularly those outlined by the CFD Vision 2030 Study [23]. Venditti and Darmofal [24] performed isotropic mesh adaption for inviscid flows in two-dimensions for multiple test cases using the finite-volume solver FUN2D. Objective function adaption was compared to Hessian-based adaption, showing that adapting to an objective function allows for more accurate representation of flow physics and force coefficients, regardless of the quantity included in the objective function, indicating the importance of a single feature on the entire flow. Venditti and Darmofal [25] expanded this adaption method comparison to include two-dimensional viscous flows on anisotropic computational meshes.

1.2.4 Design Optimization Coupled with Adaptive Mesh Refinement

Nemec et al. [26] performed inviscid design optimization coupled with adaptive mesh refinement on a finite-volume, Cartesian cut-cell computational mesh. Nemec demonstrated that without the use of error estimators to adapt the computational mesh, discretization errors can lead to non-optimal designs. Nemec saw the largest speed increase by limiting the complexity of the computational mesh initially during the design optimization, and refin-

ing the computational mesh as the design neared the targeted inverse design. Anderson [3] continued this work by performing the AIAA ADODG cases 1-4. Anderson showed as good or superior drag reduction to previous work, much of which does not include error control via adaptive mesh refinement. As an aside, Anderson's viscous cases from the AIAA Aerodynamic Design Optimization Discussion Group were initially designed inviscidly, then computed on viscous computational meshes, still demonstrating drag reductions. Dalle and Fidkowski [27] performed multi-fidelity, two-dimensional viscous and inviscid design optimization coupled with adaptive mesh refinement using a Discontinuous Galerkin method. The multi-fidelity technique was similar to the technique used for complexity control by Nemec [26]. A decrease in computational time by an order of magnitude occured using adaptive computational meshes over fixed computational meshes, coupled with a greater reduction in drag. Employing FUN3D for a fully viscous solution, using the Spalart-Allmaras turbulence model, on a quarter sector mesh of a jet nozzle, Heath [28] noted a decrease in the overpressure signature in the more optimal design, as well as an increase in overall thrust. A frozen viscous sublayer was used during the adaption process to ensure proper sublayer capture.

References [29–37] document work on problems from simple elliptic equations to complete Navier-Stokes equations using finite-element methods. This research provides a mathematically rigorous starting point for moving to finite-volume applications. With the inclusion of these articles, the hope is to take much of the rigor learned from the finite-element methods and applied for future research on automating the process. It is interesting to note that many of these references document work which was done in the early 2000's, which are not referenced in any of the finite-volume or finite-element work applied more directly to realistic aerospace problems.

Chapter 2

Methodology

This thesis attempts to validate the benefits of coupling design optimization with adaptive mesh refinement. In this section, the following items are discussed to provide background on the tools and methods that are used in this research:

- Computational mesh generation
- Optimization procedure
- Optimization strategies

2.1 Computational Mesh Generation

The current best practice for design optimization use fixed-complexity computational meshes, as the use of mesh adaption is generally reserved for final designs. A fixed-complexity mesh is a mesh that does not change in number of nodes or cells during the optimization process. This provides the baseline for the comparison with adapted computational meshes in this research. These computational meshes were created using Pointwise [38], a commercial computational mesh generation software package. A family of h-refined computational meshes were created for each baseline test case. H-refinement divides the surface edge in half,

creating a finer computational mesh at each level. Figure 2.1 is a depiction of the family of h-refined meshes, the coarsest on the left, and moving to the right, each mesh having twice as many surface nodes as it progresses and quadruple the volume nodes.

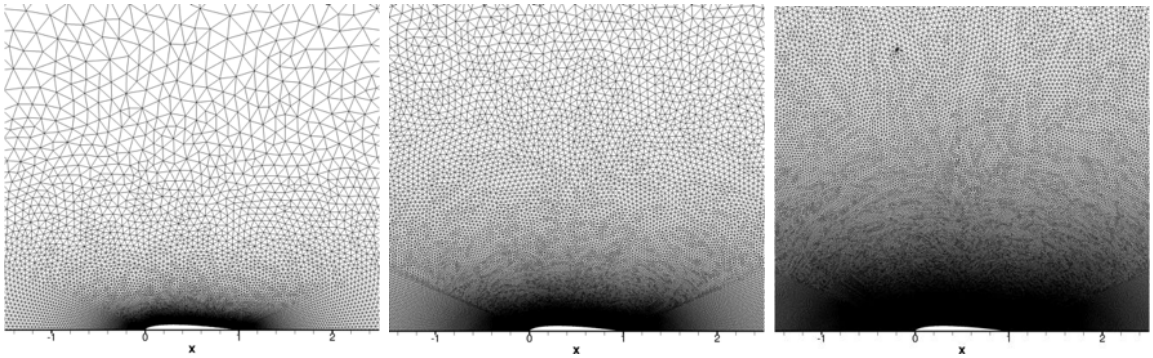

(a) Coarse (b) Medium (c) Fine

Figure 2.1: Family of fixed-complexity computational meshes

2.1.1 Collared Computational Mesh Design

The collared mesh technique acts as a form of volume sourcing for computational mesh creation. Figure 2.2 is a sample collared mesh, with the collar rings highlighted. Volume sourcing is a process of inputting control locations to help with the decay of the cells as they emanate from the source (e.g., airfoil) or in this case, the progressively distant outer boundary locations. The control locations refer to points in which the initial spacing and growth rate are defined. From those points, the mesh generation algorithm creates a mesh that best fits the explicitly defined mesh generation criteria. Cell decay corresponds to the rate at which the cells increase in size at increasing distances from the sources. A collared mesh enhances the previous computational mesh by appending additional rings to the computational mesh at the outer boundary. Table 2.1 lists the node counts for each mesh boundary distance. This table illustrates an example of the quasi-volume sourcing achieved with this technique, with node count increasing at farther distances compared to the non-collared approach.

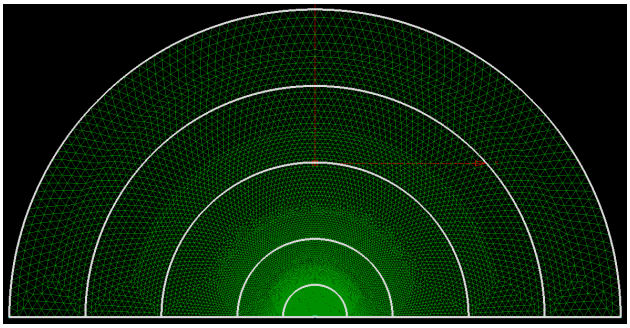

Figure 2.2: Sample collared mesh

Table 2.1: Node count for collared and non-collared meshes at various boundary far field distances

Boundary Distance	Collared Mesh Node Count	Non-Collared Mesh Node Count
5	10752	10752
10	11600	10892
25	12615	11120
50	13514	11229
75	14110	11329
100	14564	11255

For the collared approach, Table 2.2 details the spacing parameters specified for each collar at each mesh level of the family of meshes, i.e., coarse, medium, fine.

Table 2.2: Collar spacing (unit lengths)

Collar Level	Coarse Mesh	Medium Mesh	Fine Mesh
100	3.00000	1.50000	0.75000
75	2.25000	1.12500	0.56250
50	1.50000	0.75000	0.37500
25	0.75000	0.37500	0.18750
10	0.30000	0.15000	0.07500
Airfoil	0.00100	0.00050	0.00025

2.1.2 Family of Computational Meshes

The families of surface h-refined, fixed complexity computational meshes created for each test case using the collared mesh approach achieve two goals. The first is to attain mesh

convergence for the design optimization process. The second is to determine the starting surface refinement for the adaption process, i.e.,, the surface mesh points from the Medium and Fine computational meshes are selectively employed in the adaptive mesh refinement process. This avoids shape faceting, which may occur from coarse surface discretization and potentially result in sub-optimal designs, and is important for test case 1 in particular. Test case 1 was a drag reduction case for an inviscid flow, therefore all reduction in drag is reducing wave drag, and the faceting of the airfoil may introduce additional shocks. In this case, as the optimal solution removes the shock from the flow, and any sharp edges may introduce a shock.

Creation of Fixed-Complexity Computational Meshes

A family of meshes was created with target node counts for each level using Pointwise [38]. Pointwise is a mesh generation software tool that is heavily used in the CFD community. The exact details of the various settings for both fixed-complexity computational mesh test cases are detailed in their respective chapters. These families of computational meshes served as the starting point comparison for the final solution with the loosely coupled designs for both cases. This research only document comparisons using adaptive mesh refinement for the first case, as the second case was unable to obtain a reasonable adapted computational mesh given the requirement for this research to use isotropic mesh adaption. These families of computational meshes were used directly in shape optimization. To ensure fully optimized solutions, reparameterization was employed.

2.1.3 Adaptive Mesh Refinement

The mesh adaption process for this research used the "Refine/two" adaption method within FUN3D, detailed in Chapter 3. "Refine/two" does not require a frozen boundary layer mesh, allowing the adaptation to apply any changes in the shape that impact the sublayer

to the boundary layer discretization, improving the capture of the flow physics. Given the restriction placed on this research of performing only isotropic mesh adaption, no viscous mesh adaption is performed. Isotropic mesh adaption means that the cell aspect ratios are approximately 1:1. Figure 2.3 depicts the adapted mesh, with the noticeable near 1:1 aspect

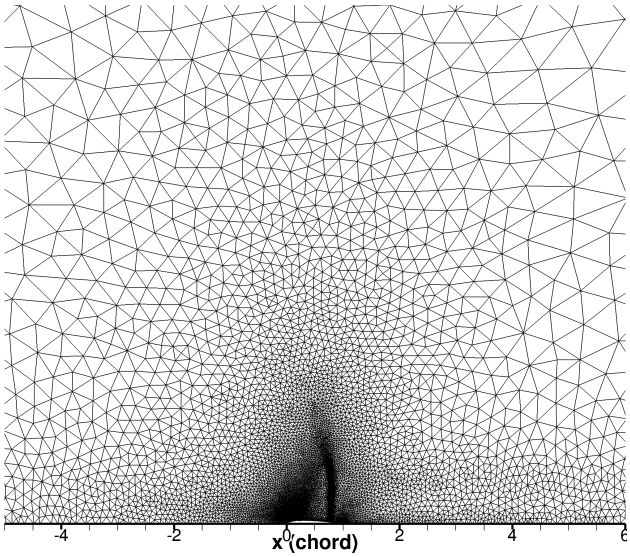

Figure 2.3: Airfoil

ratio noticeable around the edges of the picture. Figure A.1 illustrates a flow chart for the adaptive mesh refinement process within FUN3D.

2.1.4 Complexity of Computational Mesh

For this research, the number of mesh points or nodes in the 2D symmetry plane determines the complexity of the computational mesh. The 2D symmetry plane is used as FUN3D does not have a true 2D mode. FUN3D uses a "2.5D" mode, meaning the mesh is extruded 1 unit in the y direction of the mesh, as the z-direction is perpendicular to the flow direction, and the x-direction is streamwise with the flow source. When the boundary conditions are set in Pointwise, the planes at y=0 and y=1 are set to a y-symmetry condition to enact the 2D mode for FUN3D. Additionally, a flag is turned on within the FUN3D name-list

indicating that this is a two-dimensional flow to expedite the flow solution. However, this feature is unavailable in the adjoint solver, therefore requiring the use of the y-symmetry condition in the boundary condition file. Users may specify the complexity of the computational mesh in one of two ways. In the first approach, users request a desired complexity and "Refine/Two" begins making the most efficient and accurate mesh while attempting to maintain the desired complexity level. Discretization-error estimates are computed during the adapting process, allowing the user to coarsen or refine the computational mesh based on the desired discretization error. In the second approach, the user requests a discretization error tolerance and "Refine/Two" proceeds to create a mesh which meets the requested discretization error tolerance. The user may increase or decrease the tolerance during the adaption process to guide the complexity, if required.

2.2 Design Optimization

2.2.1 General Approach

The design optimization process for this research utilizes the built-in tools within FUN3D, linked to the optimizer SNOPT (Sparse Nonlinear OPTimizer) [39] for geometry modification. The process began with parameterizing the airfoil for the desired number of design variables. FUN3D then computed the flow solution, followed by the adjoint solution, and passed the sensitivities from the adjoint solution to SNOPT, which in turn determines new, more optimal design parameterization values. These values were then used to construct the new optimal airfoil shape. Figure A.2 is a flow chart depicting the process within FUN3D for design optimization.

Objective Functions

Objective functions may include a number of components, such as lift, drag, pitching moment, sonic-boom signature, and any combination of these and other values. The initial test case consists of a drag minimization problem in which the objective function is taken as the drag coefficient, C_d. For the second test case, the objective function is expressed by a penalty method. A penalty method adds a term to the objective function which increases (penalizes) the objective function value when constraints deviate from the goal, such as a target lift or pitching moment. The FUN3D mesh adaption process currently does not permit multiple adjoints for use in constrained optimization (though the design optimization does), necessitating penalty methods. This ensures the exact same optimization problem for both the fixed and adapted computational meshes. The FUN3D user manual provides the initial objective functions, modified for the unique constraints of each test case.

The objective is minimized by inputting the sensitivities into an optimization framework, which then provides shape changes based on the number of design variables and the limits on those design variables. As mentioned previously, SNOPT was the optimizer for this research. SNOPT uses sequential quadratic programming to solve nonlinear optimization problems for a given objective function and set of sensitivities. The commonality of SNOPT for aerospace design optimization problems led to its selection for this research. For all optimization calculations a single adjoint is used, as the mesh adaptation process within FUN3D does not allow for multiple adjoints. Test case 1 uses a single component objective function, unconstrained with a single adjoint for drag minimization. Test case 2 uses a two-component, penalized unconstrained objective function, with a single adjoint for drag minimization with a targeted coefficient of lift.

Parameterization

Parameterization refers to the number and location of design variables for the design optimization problem. These points may be placed throughout the aerodynamic body and provide locations for the optimizer to change the shape of the aerodynamic body.

All shape parameterizations for this research employ MASSOUD [16], a tool developed at NASA Langley Research Center by Jamshid Samareh targeted toward aerospace applications. MASSOUD generates a plane that divides the upper and lower surfaces of the aerodynamic shape, airfoils in this case, allowing for control of the deformation in aerodynamic body terms. These terms include twist, sweep, and planform shape, as well as the two terms used for this 2D research: thickness, and camber.

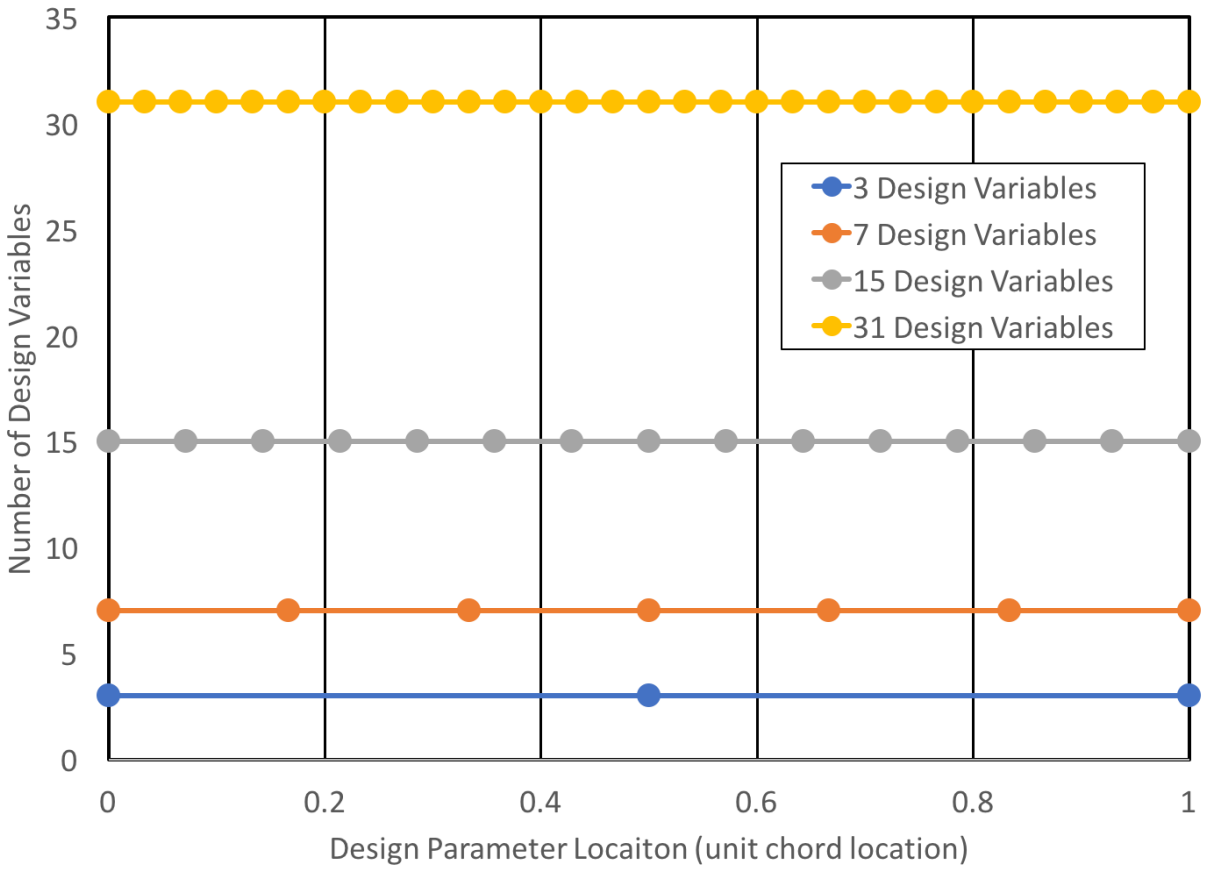

Figure 2.4: Design parameterization locations

Figure 2.4 illustrates the location of the design variables for the 4 different levels of parameterization along the unit chord length of the airfoil. These are the locations for the thickness variables for the first test case and for the thickness and camber design variables for the second test case.

2.2.2 Fixed Design Variable Parameterization

The baseline case for this research uses a fixed parameterization scheme. For the fixed parameterization approach, the number and location of design variables does not change during the optimization process. The shape is reparameterized at the end of each optimization circuit and the design process begins again to ensure a fully converged, new, more optimal design. This research uses fixed parameterizations of 3, 7, 15, and 31 design-variables, which are compared with the progressive parameterization approach described below.

2.2.3 Progressive Design Variable Parameterization

This research exploits progressive parameterization to aid in creating optimal shapes, while avoiding the introduction of irregular shape features. Progressive parameterization refers to starting with a sparse parameterization, optimizing the shape until the objective function can no longer be reduced, refining the parameterization, reparameterizing the geometry, and repeating the optimization process. Test case 1, a symmetric airfoil, uses thickness design variables, while the second test case uses thickness and camber design variables, spaced out evenly along the plane dividing the upper and lower surface of the airfoil. Two additional variables appear on each end of the thickness parameterization plane. This means that for the 3 design-variable case, there are actually 7 design-variables in the parameterization, with only 3 being active, the other 4 remaining inactive. These are not directly manipulated by the optimizer as the thickness parameterization uses a cubic polynomial.

Due to the nature of cubic polynomials, a hole may develop in the leading or trailing edge of the airfoil if the last two points in the parameterization are allowed to move freely. The progressive parameterization starts with 3 design-variables, with the final shape from the 3 design-variables reparameterized with 7 design-variables. The same reparameterization is performed after the final shapes for the 7 design-variables, 15 design-variables, and 31 design-variables, each time the parameterization is increased in design-variables.

2.2.4 Grid Complexities

Two approaches may be taken for optimizing on a fixed-complexity computational mesh. The first is to perform all optimization on a single fixed-complexity computational mesh, either using a fixed parameterization scheme or a progressive parameterization scheme. The second approach may be done two different ways. First, the optimization starts on a coarse mesh, then the resulting shape is reparameterized onto a finer mesh. This reparameterization uses the the same number of design-variables as the coarser mesh. The second method starts on a coarse mesh, with the resulting shape being reparameterized onto a finer. This reparameterization uses the next refined number of design-variables, e.g., 3 design-variables to 7 design-variables.

2.2.5 Loosely coupled adaptive mesh refinement and design optimization

This research approaches coupling of the design optimization with adaptive mesh refinement in two ways, based on whether the error estimation occurs before or after shape optimization. Within FUN3D, the error estimation occurs during the adaption process. This means that for the design followed by adaptation approach, the error estimate occurs after the optimization. Alternatively, for the adaption followed by design approach, the error esti-

mate occurs before the optimization. Micheletti [36] performed this same study using finite element methods for an advection-diffusion-reaction equation, finding that both methods reach the same solution. Figure A.3 illustrates the process for optimization-then-adaption and Figure A.4 the process of adaption-then-optimization.

2.2.6 Setting and Managing Design Variable Bounds

For thickness design parameters, the bounds define the distance that the airfoil shape may be displaced as measured from the initial parameterized airfoil surface. This is similar to the camber design parameter, with the limit now on the amount of camber displacement for the airfoil instead of the thickness displacement. Two approaches are taken for bound limits in this research. The first is to apply smaller bounds and reparameterize the shape multiple times in order to reach the final, most optimal solution. The second is to apply the largest bounds that will not cause the flow solver to fail and hold these constant throughout the entire optimization procedure. Depending on the number of design variables, even for the largest bound limits, reparameterization may be required. This will be shown in the results section of this thesis. Reparameterization refers to taking the final geometry from the design optimization procedure, inputting it into the geometry parameterization software, and using this new shape as the starting point for a new optimization. Reparameterization allows for larger effective bounds to be explored at smaller intervals. During an optimization, too large of a step within the bounds may be taken, causing the flow solver to crash, resulting in no new design. By taking smaller steps and reparameterizing at the end of each optimization circuit, the initial larger bounds may be searched successfully, just over multiple optimization circuits.

An optimization circuit is defined as the entire process from when the flow solver is used on the geometry for the first time until the optimizer, SNOPT, exits and terminates the process. This termination may be for multiple reasons, including reaching the desired optimality,

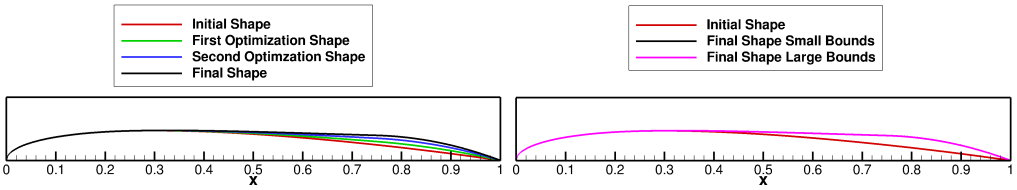

(a) Small Bounds (b) Large Bounds

Figure 2.5: Bound size comparison as it applies to reparameterization

reaching the maximum number of major design iterations, or that SNOPT has encountered numerical difficulties and is no longer able to provide a new shape for FUN3D. Figure 2.5 illustrates that the same final shape may be achieved through the use of reparameterization with a single large bound optimization circuit.

Optimality is an additional important term for this research. Optimality is defined as the degree to which the Karush-Kuhn-Tucker (KKT) [40] conditions are satisfied. As this research uses unconstrained optimization, optimality is related directly to the magnitude of the design parameter sensitivities.

2.3 Overall Strategies

This research uses the following cases to demonstrate the benefits of coupling mesh adaption with design optimization:

- Fixed bounds on a fixed-complexity computational mesh with fixed parameterizations (Baseline)
- Variable bounds on a fixed-complexity computational mesh with fixed parameterizations
- Variable bounds on a fixed-complexity computational mesh with progressive parameterization

- Variable bounds on a discretization-error-adapted computational mesh with fixed parameterizations
- Variable bounds on a discretization-error-adapted computational mesh with progressive parameterization

To justify the benefits of the coupled mesh adaption and design optimization, the following values will be used as comparison points:

- Final value of the objective function
- Complexity of the computational mesh
- Optimization Complexity Function (O.C.F.) defined as:

$$O.C.F. = L^2 * \sqrt{0.1 * F.S.C. * 10 * O.C. * 0.01 * M.C.} \tag{2.1}$$

  - This is a combination of the objective function (L), the number of flow solution calls (F.S.C), optimization circuits (O.C.), and the complexity of the computational mesh (M.C.). This is chosen to provide a relative speed term to the optimization process as the optimization circuits were performed on three different machines, all with different clock speeds and number of cores per node. The more efficient optimization process tends to a value of zero for the O.C.F.. The coefficients were chosen to reflect the fact that the user interaction required with new optimization circuits is more costly for this research compared to the other items. These coefficients may be adjusted for each individual research problem depending on how the critical computing sources are for the research.

Chapter 3

Numerical Approach

During this research, many tools have been used to enable the optimization process, as well as to carry out the workload. Practices in current research and industry fields provide a guideline for tools aiding and expediting numerical processing, helping to reduce workload as well as required computational time and resources. This research employs the following software and machines for this purpose.

3.1 FUN3D

FUN3D [41] is a second order, finite-volume, node-centered computational fluid dynamics solver developed and maintained at NASA Langley Research Center. FUN3D solves the Euler and Reynolds Averaged Navier Stokes (RANS) equations for both compressible and incompressible flows on unstructured computational meshes. For the first test case of in this research, the compressible Euler equations are used. For the second test case, the compressible RANS equations with the Spalart-Allmaras [42] turbulence model equations are used. The RANS optimization is limited to the Spalart-Allmaras model, as it is the only turbulence model with an adjoint solver within FUN3D. FUN3D has many options for turbulence modeling, inviscid flux implementation, and flux limiting; however, for this

research, the following options were chosen: Vanleer flux vector splitting method for inviscid flux construction for both the residual and Jacobian constructions, and GMRES with 2500 Krylov vectors for the inviscid test case and 1000 Krylov vectors for the RANS case. All cases are attempted to be converged to a RMS residual drop of 10E-13, providing fully converged solutions for the adjoint solver, design optimizer, and mesh adaption.

3.1.1 Flow Solver

A custom version of FUN3D was compiled for this research. This is due to an error within SNOPT which producing a failure when reading the specified optimality value from an input file. The custom version set the optimality tolerance within FUN3D, which is hard coded, to 1E-40. The low optimality tolerance assures that SNOPT and FUN3D continue exploring the design space within the predefined bounds fully without encountering a premature convergence tolerance.

3.1.2 Adjoint-Based Design Optimizer

To perform optimization within FUN3D, three folders are required: ammo, model.$\boldsymbol{n}$, and description.$\boldsymbol{n}$.

The ammo folder contains the files required for job submission script, the design name-list, and the optimization script which controls the sequencing of the required elements of FUN3D for design optimization. The required elements include the flow solver, adjoint solver, sensitivities calculations, optimizer, and mesh motion. The design name-list dictates which optimizer to use, the location of the computational mesh to be optimized, as well as other options. The optimizer tied to the code is SNOPT [39].

The model.$\boldsymbol{n}$ folder contains the final optimized shape, as well as a shape history, sensitivity history, and a forces history. The $\boldsymbol{n}$ indicates the point for the optimization in a

multi-point optimization if that is desired. For this thesis, all $\boldsymbol{n}$'s are 1, as no multi-point optimization is performed.

The description.$\boldsymbol{n}$ folder contains the computation mesh, design optimization parameterization, the flow solver name-list, and the file containing the objective function and bounds for the optimizer to move the parameterization.

All three folders are required for design optimization. The path for the parent folder for these three folders is set in the design name-list.

3.2 Mesh Generation

Computational meshes are generated with Pointwise Version 17 [38], an industry standard for mesh generation and provides acceptable starting meshes for the adaption process. Using best practices with aid from NASA Langley's Geolab, fixed complexity computational meshes are generated for the comparison to the adapted computational meshes using Pointwise. All computational meshes are generated with the built-in Advancing Front, inviscid generation method. Boundary decay values are determined by trial and error to the desired node count for each level of the fixed computational meshes. The adapted computational meshes are started with the coarse level fixed computational mesh.

3.3 Data Reduction

Data is reduced and analyzed using Tecplot360. Tecplot360 is a post-processing visualization tool and an industry standard. Flow field and computational mesh visualizations are created with Tecplot360, and layout files are developed to ensure the consistent features are presented for each case. Surface pressures and convergence data are created from Tecplot360 as well, as it produces acceptable plots and allows for a single post-processing tool for all

aspects of data reduction and visualization.

3.4 Computational Power

NASA Langley Research Center's K-Cluster [43] is the computational resource used for all FUN3D cases in this thesis. The K-Cluster is comprised of three different machines: K2, K2a, and K3, each of which are described in Table 3.1

Table 3.1: Computational resources used for research

Name	Machine Type	Number of Nodes	Number of Cores	Core Description	Node Memory
K2	SGI ICE Altix 8400	160	1920	Dual socket hex core 3.07 GHz	24GB RAM per node
K2a	IBM iDataplex	252	3024	Dual socket hex core 2.80 GHz	24GB RAM per node
K3	SGI ICE Altix X	262	4192	Dual socket oct core 2.60 GHz	32GB RAM per node

Chapter 4

Results for Test Case 1: Transonic, Inviscid, Non-lifting, Drag Minimization

Test case 1, taken from the AIAA Aerodynamic Design Optimization Discussion Group (ADODG) [2], consists of a drag optimization on a NACA 0012 airfoil while maintaining symmetry and thickness no less than 12%. This case has a theoretical minimum C_d of 0 shown by Spalart [44], achieved by rounding the trailing edge and blunting the leading edge. Work by Li [1] and Anderson [3] provides a comparison for FUN3D to other flow solvers for both fixed-complexity computational meshes and discretization-error-adapted computational meshes. Li achieved a minimum drag of 100 counts using PADGE, the DLR DG solver [45], and Anderson reduced the drag to 43 counts with CART3D [4]. Both cases adapted the mesh using element or cell subdivisions. Furthermore, Li performed p-refinement mesh adaptation with comparison to a family of fixed-complexity computational meshes. Similar comparisons with multiple parameterization techniques and methods on both fixed-complexity computational meshes and discretization-error adapted computational meshes are performed in

this research. The objective function is taken as the drag coefficient on the airfoil which is obtained as twice the value of the integrated drag on the half symmetric airfoil profile.

4.1 Problem Description

This research uses the modified NACA 0012 [2] airfoil geometry prescribed by the AIAA ADODG in Equation 4.1.

$$y = 0.6 * (0.2969 * \sqrt{x} - 0.1260 * x - 0.3516 * x^{+}0.2843 * x^3 - 0.1036 * x^4) \tag{4.1}$$

The modification closes the trailing edge to a sharp point. All computations are performed on a half mesh to take advantage of the requirement for symmetry and speed up computation time. Figure 4.1 depicts an example of a half mesh.

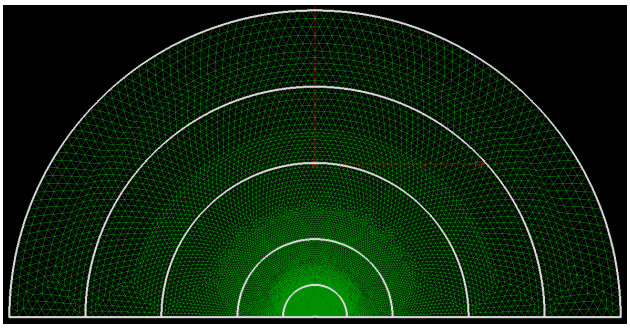

Figure 4.1: Sample half mesh

4.2 Solver Setup

This research uses the following non-default FUN3D settings to converge the problem:

- Compressible, inviscid flow equations
- Mach 0.85

- Objective function L = C_d
- Van Leer flux vector splitting is used for both the residual and Jacobian inviscid flux construction
- Residual stopping criteria of 1E-13 for the flow, and adjoint solvers to ensure that the Hessian is accurately approximated as possible within SNOPT
- Mesh movement residual stopping criteria of 1E-13 for the mesh movement equations to reduce the likelihood of negative volumes. By reducing the likelihood of negative volumes, the bounds may be larger which results in a lower number of optimization circuits.
- SNOPT Optimality stopping criteria is set to 1E-40 to ensure a fully converged design problem without an early exit. This is a hard-coded limit in FUN3D. It must be hardcoded as there is a bug within SNOPT that does not allow it to read in an optimality tolerance from an input file.
- A maximum of 2500 Krylov Vectors are used for the flow solver and adjoint solver. This is not a default option for FUN3D, but it allows for increased CFL ramping and consistent convergence for every flow solver and adjoint solver evaluation. By using this large number of Krylov vectors, memory becomes an issue for the adjoint solver in particular, so this method may not be appropriate for larger, 3D cases.

These solver settings help expedite the residual convergence and design optimization process. Initial testing of the design cases determined these settings before work on this research began.

4.3 Fixed-Complexity Computational Mesh Generation

A family of meshes was created with target node counts for each level using Pointwise. Table 4.1 details the settings used in Pointwise to create the meshes. These use the collared mesh approach detailed in Chapter 2. The boundary decay feature within Pointwise, a value that varies from 0 to 1, controls how quickly the cells grow as the advancing front of the computational mesh approaches the boundaries. A higher value corresponds to less growth. The airfoil spacing refers to the node spacing on the airfoil, being non-dimensionalized by the airfoil chord length

Table 4.1: Pointwise settings for test case 1

Mesh	**Boundary Decay**	**Airfoil Spacing**	**Node Count**
Coarse	0.9875	0.001	49804
Medium	0.99715	0.0005	199284
Fine	0.99929	0.00025	801073

Table 4.1 gives the quantities for the controllable features within Pointwise used to create the family of fixed-complexity computational meshes. These settings may be used in combination with the collared mesh approach to recreate these meshes.

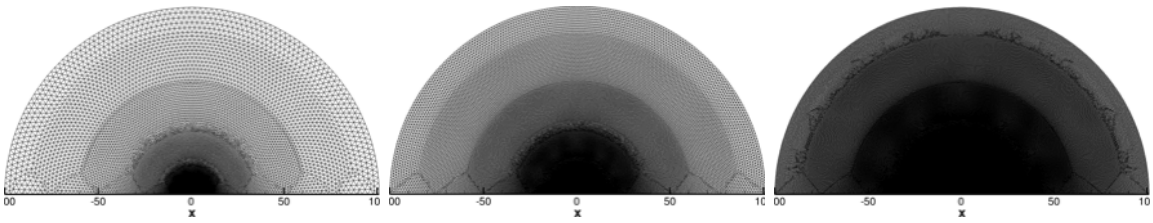

(a) Coarse (b) Medium (c) Fine

Figure 4.2: Overall view of fixed-complexity computational meshes

Figures 4.2 through 4.5 depict the family of fixed-complexity computational meshes and allow for visualization of the collaring effects. A computational mesh convergence study was performed to determine the reference baseline drag value for the NACA-0012 airfoil. Figure

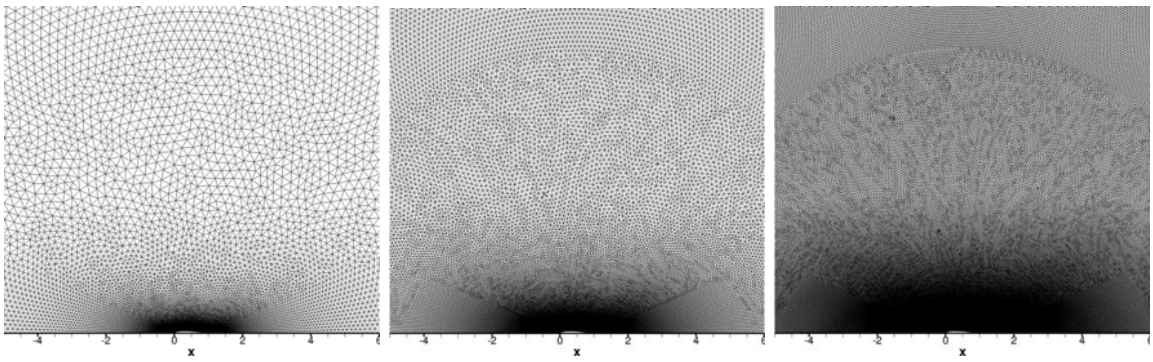

(a) Coarse (b) Medium (c) Fine

Figure 4.3: Zoomed view of fixed-complexity computational meshes

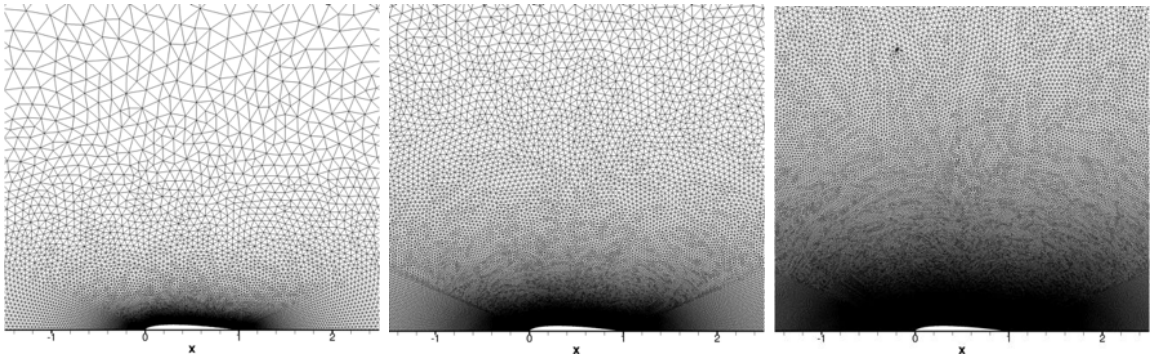

(a) Coarse (b) Medium (c) Fine

Figure 4.4: Near-field view of fixed-complexity computational meshes

4.6 is the drag convergence plot for the family of fixed-complexity computational meshes. The straight-line behavior of Figure 4.6 is indicative of consistent grid convergence and second-order accuracy. The computed drag of the nominal airfoil on the fine fixed-complexity computational mesh is 470.84 counts. Extending this plot to the y-intercept (1/nodes = 0) gives the infinite resolution drag value of 470.82 counts, which is within two one-hundredths of a count of drag of the fine fixed-complexity computational mesh. Figure 4.7 depicts the Mach contours for the coarse, medium, and fine fixed-complexity computational meshes, showing that as the mesh is refined, the shock resolution becomes sharper. Figure 4.8 shows the computed surface pressure coefficient for the family of fixed-complexity computational

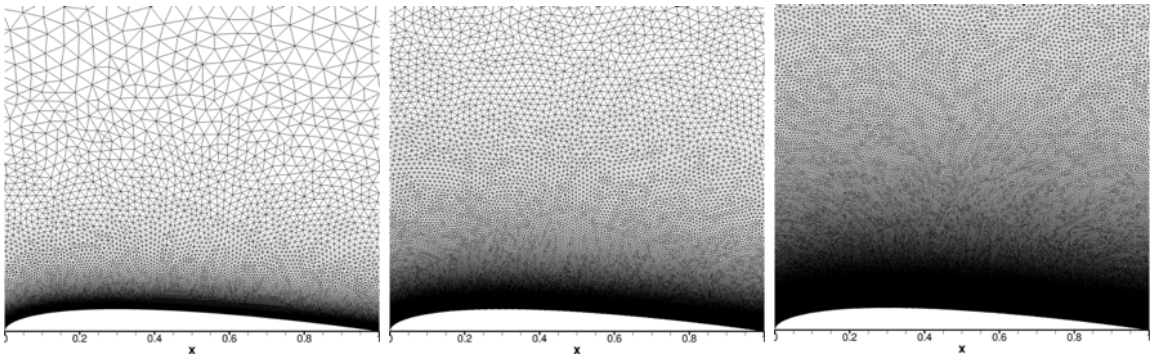

(a) Coarse (b) Medium (c) Fine

Figure 4.5: Airfoil view of fixed-complexity computational meshes

meshes. The shock occurs at approximately the 0.75 chord location. Figure 4.9 is a closer inspection of shock location, showing that refining the mesh sharpens the shock and shock location.

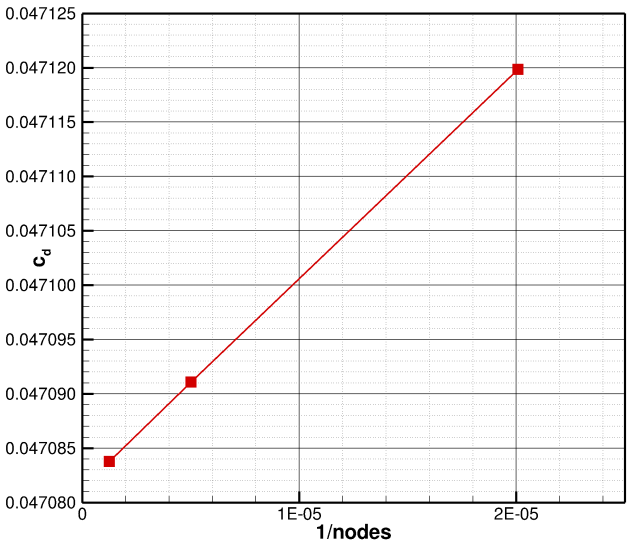

Figure 4.6: Drag convergence for the fixed-complexity computational mesh on the initial shape of a NACA-0012m

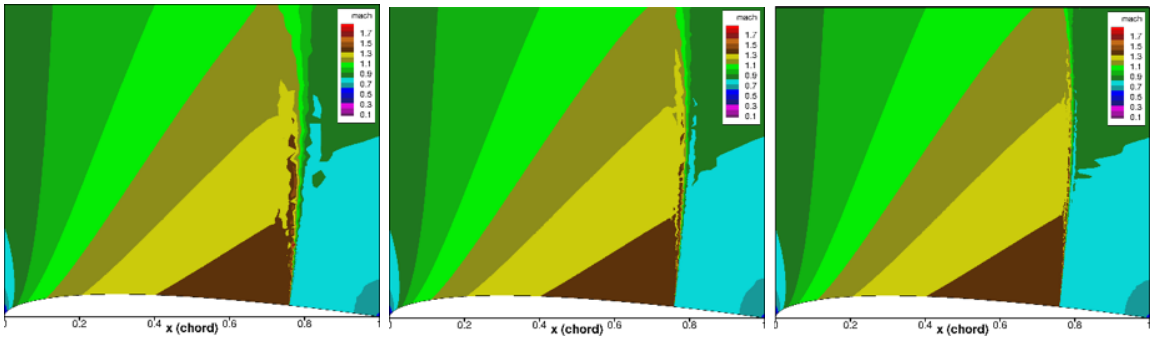

(a) Coarse (b) Medium (c) Fine

Figure 4.7: Mach convergence for the family of fixed-complexity computational meshes

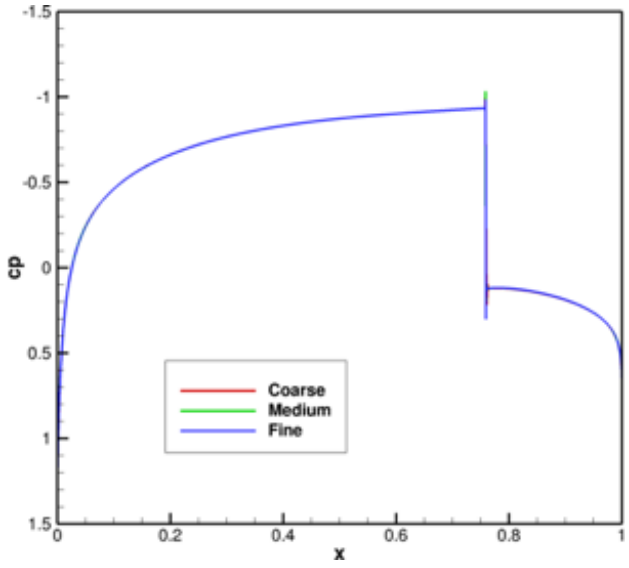

Figure 4.8: Surface coefficient of pressure profiles for the family of meshes

4.4 Fixed-Complexity Computational Mesh, Fixed Parameterization Results

4.4.1 Three design-variable

For the 3 design-variable case, and for all the fixed parameterization cases, the optimization process started with the NACA-0012 airfoil, optimizing until the output values leveled off at a final design value and the optimality decreased at least 3 orders of magnitude.

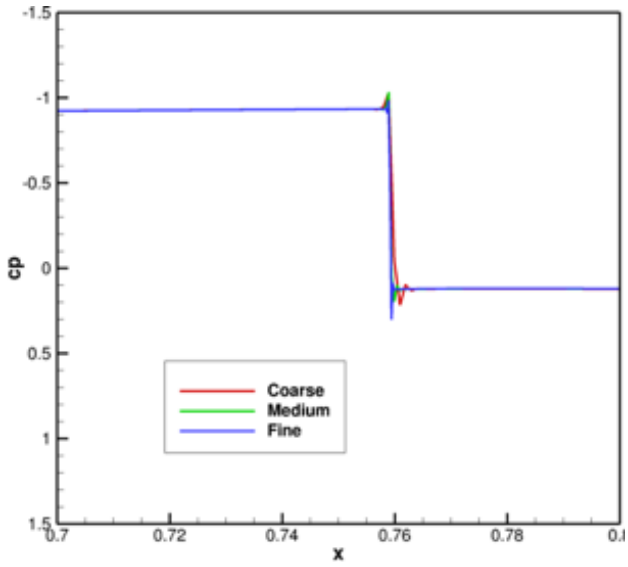

Figure 4.9: Shock location view of surface coefficient of pressure

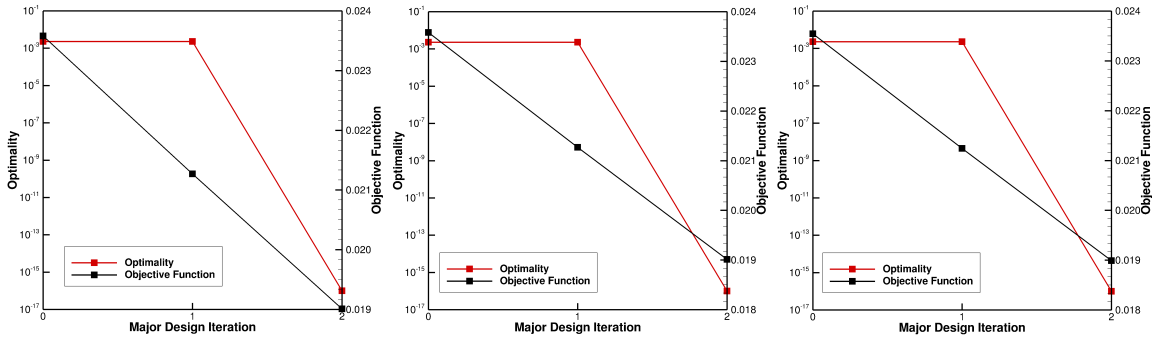

(a) Coarse (b) Medium (c) Fine

Figure 4.10: Optimality, and objective function convergence from SNOPT for the family of fixed-complexity computational meshes with 3 design-variable for the first optimization circuit

Figure 4.10 shows the optimality convergence of the first optimization circuit for the family of fixed-complexity computational meshes. As defined in Chapter 2, an optimization circuit corresponds to the entire process from when the flow solver is used on the geometry for the first time until the optimizer, SNOPT, exits and terminates the process. For the first optimization circuit, all computational meshes reached machine precision for optimality and all cases yielded approximately 380 counts of drag, a reduction of 90 counts. The upper

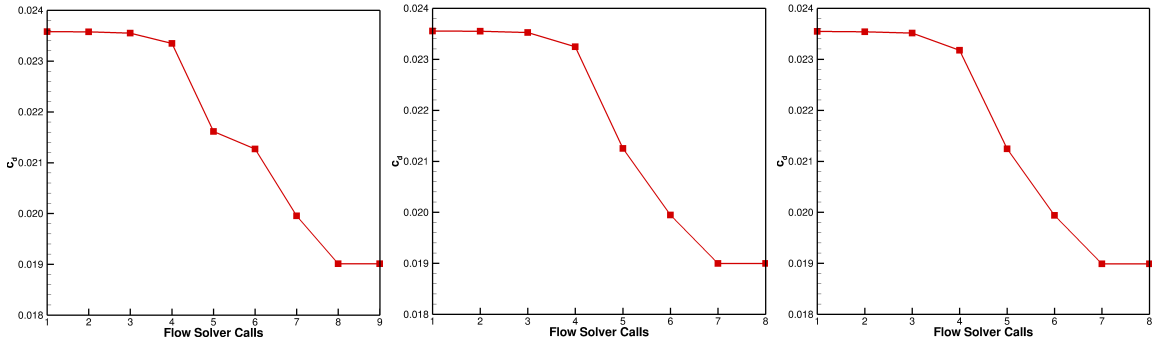

(a) Coarse (b) Medium (c) Fine

Figure 4.11: Flow solver call convergence for the family of fixed-complexity computational meshes with 3 design-variable for the first optimization circuit

bounds for the design variables during this optimization were set to 0.01. This is uniform for all three fixed-complexity computational meshes and for all numbers of design variables to ensure equal comparison throughout the optimization process for an optimization baseline. Figure 4.11 shows the convergence of the optimization problem as a function of flow solver calls during the first optimization circuit. The medium and fine mesh converge almost identically, with the coarse mesh requiring one more iteration.

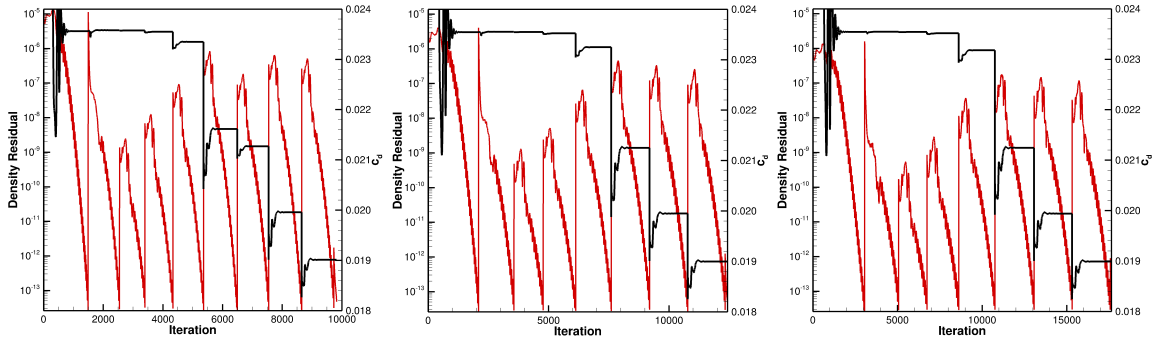

(a) Coarse (b) Medium (c) Fine

Figure 4.12: Family of fixed-complexity computational meshes density (rho) residual convergence (red line) and drag values flow solution (black line) convergence history for 3 design-variable first optimization circuit

Figure 4.12 depicts the density residual convergence and drag value for the flow solver during the first optimization circuit for the coarse, medium, and fine 3 design-variable fixed-

complexity computational meshes. All flow solver calls during the optimization circuit converge to machine precision. This convergence has lead to more rapid and consistent design optimization, and is prescribed to ensure no discrepancies arise from the incomplete convergence of the flow solution or adjoint solutions.

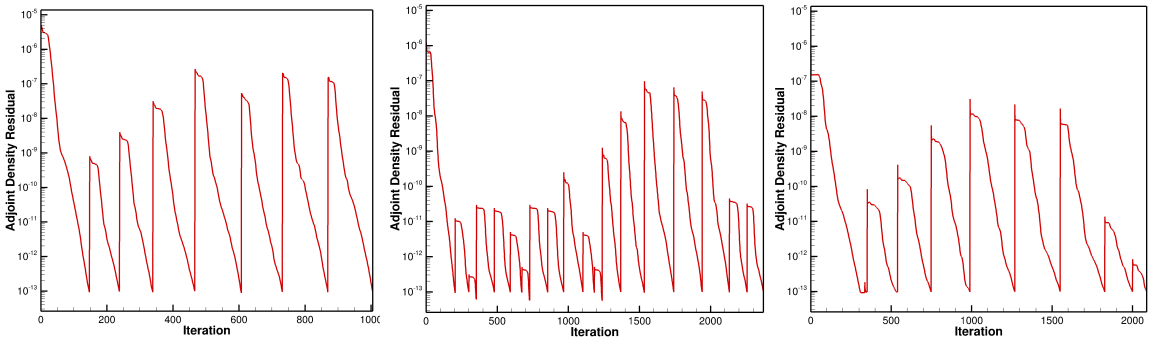

(a) Coarse (b) Medium (c) Fine

Figure 4.13: Family of fixed-complexity computational meshes density (rho) adjoint residual convergence

Figure 4.13 details the adjoint convergence for the coarse, medium, and fine meshes. It confirms that all adjoint residual values reached machine precision, ensuring optimization differences from residual convergence are reduced and do not affect the design outcome.

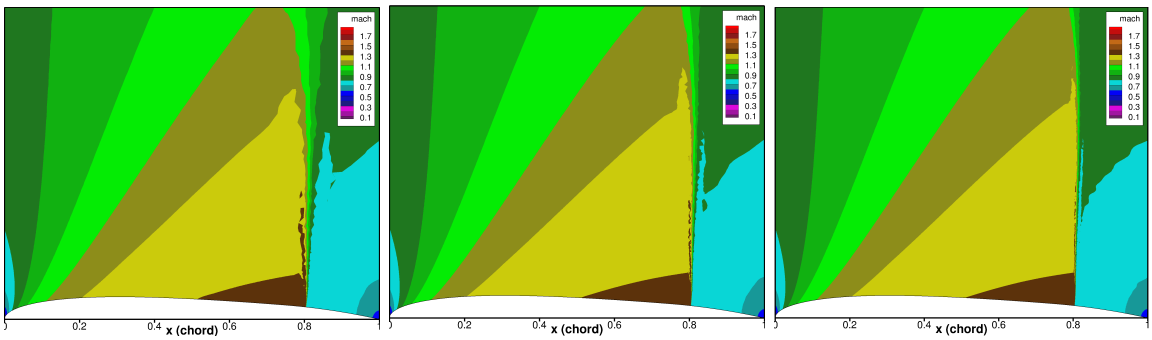

(a) Coarse (b) Medium (c) Fine

Figure 4.14: Mach contours with 3 design-variable for the first optimization circuit

Figure 4.14 illustrates the Mach contours for the resulting shape from the first optimization circuit, with the shock moving aft approximately 0.05 chord length. Table 4.2 details

Table 4.2: 3 design-variable first optimization circuit tabulated values

Mesh	Flow Solver Calls	Objective Function: C_d	Optimality	Optimization Complexity Function
Coarse	9	0.038022	1e-16	0.09679
Medium	8	0.037994	1e-16	0.18227
Fine	8	0.037980	1e-16	0.36517

the final values of the first optimization circuit. All three fixed-complexity computational meshes reached machine zero for optimality, with the coarse computational mesh requiring one more flow solver call during the optimization process. The trend seen in the baseline airfoil data continues, where the coarse mesh is highest in drag and the fine is the lowest. Even though the fine and medium computational meshes produce a lower drag value, the O.C.F. does indicate more efficiency from the coarse computational mesh. This efficiency comes from the overall cost for the solution. This does not include the number of cores or nodes, as the speed of the cores vary across machines and can impact the overall time of the solution. These values are for the first optimization circuit of the 3 design-variables case.

Table 4.3 documents the final results from the 3 design-variable design problem using the full set of optimization circuits. This differs from Table 4.2 in that it includes all final values for the 3 design-variable problem. To reach the values in Table 4.3, 3 reparameterizations are required, which leads to 4 optimization circuits (including the initial parameterization). Reparameterizing the final design at the end of an optimization circuit creates new effective bounds. The coarse computational mesh required 4 optimization circuits to reach an optimality of machine precision and a converged objective function. These additional circuits are required to further reduce the objective function and to bring the optimality back to machine precision. The medium and fine computational mesh use the same number of optimization circuits as their stopping criteria to ensure a consistent comparison of the final design at each mesh level.

Table 4.3: 3 design-variable final design tabulated values

Mesh	Optimization Circuits	Flow Solver Calls	Objective Function: C_d	Optimality	Optimization Complexity Function
Coarse	4	48	0.029248	1e-16	0.26453
Medium	4	48	0.029194	4.5e-8	0.52720
Fine	4	78	0.029152	7.7e-10	1.34354

Table 4.4: 7 design-variable final design tabulated values

Mesh	Optimization Circuits	Flow Solver Calls	Objective Function: C_d	Optimality	Optimization Complexity Function
Coarse	7	221	0.013624	1e-16	0.16292
Medium	7	269	0.013606	1.5e-6	0.35861
Fine	7	277	0.013598	1.2e-8	0.72874

4.4.2 Seven Design Variables

The 7 design-variable case reduced the drag of the baseline airfoil by approximately 330 counts. Again, the number of optimization circuits required for the coarse mesh to reach machine optimality convergence was used for the stopping point for the medium, and fine computational meshes.

Table 4.4 details the final totals for the 7 design-variable fixed parameterization design problem for the family of fixed-complexity computational meshes.

4.4.3 Fifteen Design Variables

Fixed complexity results are only discussed for the coarse mesh for the 15 and 31 design-variable cases, as well as the progressive parameterization design cases. This is for two reasons: the first that it has been shown that the medium and fine mesh follow the logical trend of coming to slightly lower drag values than the coarse mesh. The second is that the required number of optimization circuits and flow solver calls for the next cases become too

computationally expensive given the available resources.

During the optimization process, an increase in the drag was observed as optimization circuits were performed. After investigating the airfoil shape and the upper surface integrated pressure values, it was seen that the trailing edge of the airfoil continues to become blunt. This movement continues to advance the airfoil shape towards the expected optimal design, which has been shown by Spalart [44] and other researchers for this design problem. More evidence is provided in the 31 design-variable case. This may provide insight for other design problems. Though the objective function may increase in value between circuits, it eventually decreases and reaches a more optimal solution overall. These paths should be investigated by the optimizer as they may show a more globally optimal shape than initially considered.

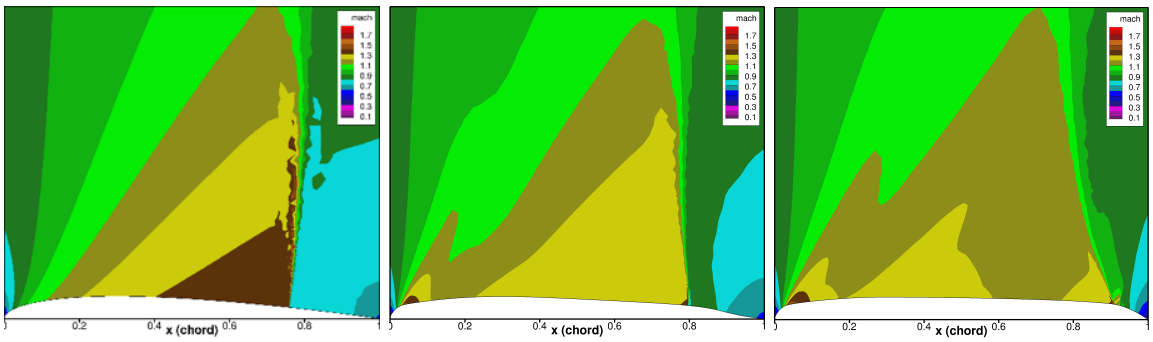

(a) Initial (b) Optimization Circuit 1 (c) Optimization Circuit 4

Figure 4.15: Mach convergence for successive optimization circuits

Figure 4.15 shows changes in design shapes between the initial shape and optimization circuits 1 and 4. The airfoil thickness increases near the trailing edge after the initial optimization circuit created a "dove-tail". This initial "dove-tail" takes multiple optimization circuits to remove before the rounded trailing edge develops.

Table 4.5 documents the final set of results for the 15 design-variable fixed parameterization case. Note that the optimality did not decrease by the desired 3 orders of magnitude, but drag was reduced by over 400 counts and the final design-variable values were not near the edge of the bound limits.

Table 4.5: 15 design-variable final design tabulated values

Optimization Circuits	Flow Solver Calls	Objective Function: C_d	Optimality	Optimization Complexity Function
17	472	0.005898	8.3e-2	0.06954

4.4.4 Thirty-One Design Variables

Similarly to the 15 design-variable case, the 31 design-variable shape develops a more rounded trailing edge as the optimization circuits progress. This exhibits the same occasional increase in drag between circuits, but overall comes closer to the analytic solution of a vanishing drag value.

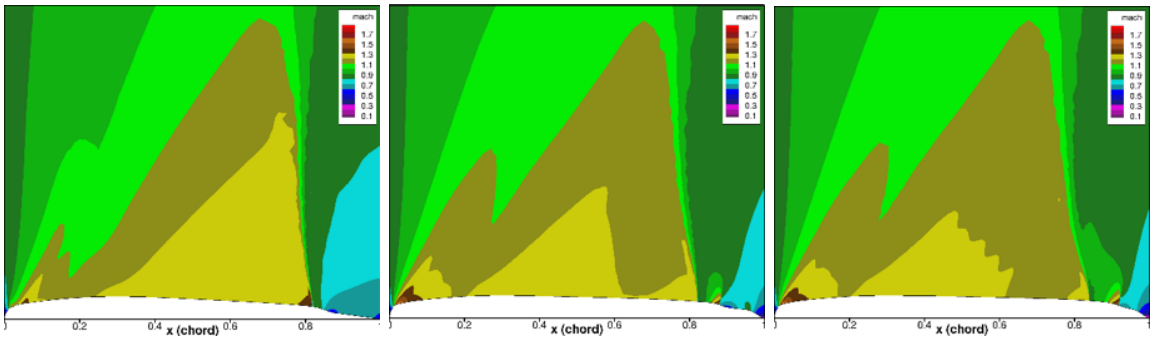

(a) Optimization Circuit 1 (b) Optimization Circuit 9 (c) Optimization Circuit 14

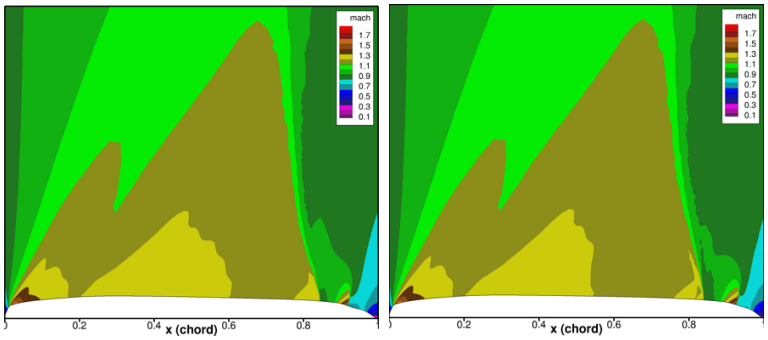

(d) Optimization Circuit 15 (e) Optimization Circuit 16

Figure 4.16: Mach convergence for successive optimization circuits

Figure 4.16 illustrates a more pronounced "dove-tail" in the 31 design-variable case, emphasizing its movement aft as the design problem is reparametrized and re-optimized.

Table 4.6: Select 31 design-variable optimization circuit tabulated values

Optimization circuit #	Integrated Upper Surface Pressures	Objective Function: C_d
1	0.52697	0.023046
9	0.58760	0.015070
14	0.60389	0.012856
15	0.60542	0.013040
16	0.60951	0.012722

Table 4.7: 31 design-variable final design tabulated values

Optimization Circuits	Flow Solver Calls	Objective Function: C_d	Optimality	Optimization Complexity Function
28	926	0.004146	7.6e-8	0.06177

Table 4.6 details the values of the shape change, showing an increase in drag between optimization circuit 14 and 15, but also an increase in the integrated upper surface pressure. This may suggest there was an increase in the area under the curve, the airfoil shape in this case, and the design was approaching the more optimal shape. The increase in drag is attributed to the larger shock forming over the aft portion of the airfoil as the shape changes. The change between optimization circuit 15 and 16 shows another increase in the integrated upper surface pressures and a decrease in the overall drag of the shape, indicating the new shape reduces the shock strength.

Table 4.7 details the final tabulated values for the 31 design-variable design problem. This reduced the drag the most out of all the fixed parameterization cases but came at the highest cost for flow solver calls and optimization circuits.

For the final optimization circuit, the bound was tightened to 0.0005 chord lengths. This was done to reduce stalling in the flow solver residuals seen for the final optimization circuit for the original bounds of 0.01. By reducing the bound sizes after the final reparam-

Table 4.8: Maximum bound limit, fixed parameterization tabulated final values for fixed-complexity computational meshes

Design Variables	Optimization Circuits	Flow Solver Calls	Objective Function: C_d	Optimality	Optimization Complexity Function
3	1	21	0.029246	1.7e-5	0.08747
7	1	72	0.013620	4.3e-7	0.03513
15	5	573	0.004044	3.4e-6	0.01954
31	18	677	0.004075	5.1e-8	0.04091

eterization, the optimizer has a much smaller search region and the optimizer explores the design space much more rapidly and converges to a final solution more rapidly as well.

4.4.5 Fixed-Complexity Computational Mesh, Fixed Parameterization, Max Bounds

One method for counteracting the increase in optimization circuits required to reach the minimum drag is by utilizing larger bounds. For this design problem, the bounds were increased to the largest values that did not cause the flow solver to fail before completion for each optimization circuit. A disadvantage of this approach that there is a great deal of trial and error and human interaction to determine the bound limit values. Table 4.8 details the final values for this maximum bound design case. The 3 design-variable case reaches the design solution in 21 flow-solver calls, 27 less than the in the smaller bound limit design problem described above, and in one optimization circuit, further reducing user interaction. The 7 design-variable case further reduces dramatically the number of flow solver calls and optimization circuits. The optimization circuits decrease from 7 to 1, and the flow solver calls decrease from 221 to 72. These reductions in flow solver calls and optimization circuits continues in the 15 and 31 design-variable cases.

A second optimization circuit was performed on both the 3 and 7 design-variable cases.

When the second optimization circuit was run, the optimality reaches 1e-16 with no change in drag; therefore, only one optimization circuit is necessary. The bounds for the 3 design-variable case were 0.5. This allows the optimizer to move the design-variables around and search more of the design space. For the 7, 15, and 31 design-variable case, the bounds were set to 0.05. This still allowed for much of the design space to be searched, but this does show that with fewer design-variables, more of the design space may be searched earlier. For the 15, and 31 design-variable cases, the bounds had to be decreased after the second optimization circuit to 0.01, as the flow solver would crash from instabilities in the solution process.

4.5 Fixed-Complexity Computational Mesh, Progressive Parameterization

A progressive parameterization scheme is used to further improve upon designs and expedite the design process, in terms of reduced number of flow solver calls and optimization circuits. This method allows for the major design changes to occur with fewer design variables. This can expedite the design process by using the coarser parameterization for the larger changes and then using the finer parameterizations for the final optimizations of the design. The two different approaches for the bound limit values are used in the progressive parameterization method. These are the fixed and max bounds, the same fixed and max bound cases from the fixed-parameterization cases.

4.5.1 Fixed Bounds

Starting with the converged solution of the 3 design-variable case from the fixed bounds, fixed parameterization case, the resulting shape is reparameterized with progressively more

Table 4.9: Progressive design variable parameterization tabulated values fixed mesh case

Design Variables	Optimization Circuits	Flow Solver Calls	Objective Function: C_d	Optimality	Optimization Complexity Function
3	4	48	0.029248	1e-16	0.26453
7	4	216	0.013956	1.9e-5	0.12776
15	6	166	0.006396	1.2e-9	0.02881
31	10	400	0.004442	1.6e-5	0.02785

(7, 15, 31) design variables, with the same fixed bounds of 0.01. Table 4.9 details the final tabulated values for each stage of the progressive parameterization for the fixed bounds. An additional 4 optimization circuits were required to drop the drag to approximately 139 counts. While this is 2 counts higher than the fixed 7 design-variable case, both are still far from optimal. When the 7 design-variable case had converged, the shape was reparameterized with 15 design-variables. The 15 design-variable parameterization was able to reduce the drag by over 50% from the final solution of the 7 design-variable case. The final 15 design-variable solution was within 6 counts of the fixed-parameterization value for 15 design-variables, and was achieved in 11 fewer optimization circuits.

With 31 design-variables, the remaining drag is reduced by approximately 33%, with 10 additional optimization circuits. The total number of optimization circuits is 24, which is 4 less than the number required for the 31 design-variable case. The final drag value is within 2 counts of the fixed 31 design-variable case. This reduction in optimization circuits reduces human interaction with the design optimization process, helping to expedite the design process. While the final O.C.F. value for the 31 design-variable portion of the progressive parameterization with the fixed bounds in Table 4.9 is reduced over the fixed-parameterization 31 design-variable case in Table 4.7, the total amount of user interaction required with the reparameterization after each optimization circuit is similar.

For the progression to the 31 design-variable case, the bounds required tightening from

Table 4.10: Progressive Design Variable Parameterization Tabulated Values fixed mesh case, max bounds

Design Variables	Optimization Circuit	Flow Solver Calls	Objective Function: C_d	Optimality	Optimization Complexity Function
3	1	21	0.029246	1.7e-5	0.08747
7	1	26	0.013646	4.6e-10	0.02119
15	11	364	0.007244	1.7e-5	0.07410
31	7	321	0.003858	5.9e-7	0.01575

the initial value of 0.01 to 0.005, and then to 0.0025. The reason for this is that when the bounds stay at 0.01, the flow solver convergence stalls, and the design oscillates between solutions; the adjoint that is computed from the flow solution is not as accurate, as the flow solution does not converge past 1e-5 and instead oscillates until the maximum number of flow solver iterations is reached.

4.5.2 Max Bounds

By increasing the bounds for the progressive parameterization method, a final drag of 39 counts was achieved in 20 optimization circuits. The progress between each stage of the progressive parameterization is documented in Table 4.10.

The max bounds case for progressive parameterization final design outperforms that fixed bounds case, similar to the fixed parameterization cases. The final O.C.F. for the 31 design-variable case part of the max bounds progressive optimization in Table 4.10 indicates that there is an increase in performance over the 31 design-variable case in Table 4.9 from the fixed bounds progressive parameterization case. These are the final O.C.F. values, which were reached after trial and error to find the bounds that allow for a convergence optimization circuit. The bounds for the 3 design-variable case were 0.5, as it was the solution from the fixed-parameterization case. The 7 design-variable case had the bounds on the design-variables reduced to 0.02, after a trial and error process of reducing the bounds from the

0.5 to get a completed optimization circuit. The 15, and 31 design-variable cases had the design-variable bounds reduced to 0.01 for the first optimization circuit and had to be reduced to 0.0005 by the final optimization circuit for the 31 design-variable case. These reductions were done for multiple reasons, depending on the optimization circuit. These reasons include the need to reduce the flow solver stalling behavior, design-variable oscillations that cause unnecessary amounts of flow solver calls, and issues with the flow solver becoming unstable and crashing. Again, this took a much trial and error, and the final optimization circuit values for each of the design-variable parameterizations does not reflect the total amount of trials to get a completed optimization circuit.

4.6 Adapted Mesh, Fixed Parameterization Results

An additional method for reducing the required number of optimization circuits to reach the minimum drag utilizes adaptive mesh refinement techniques. For the discretization-error adapted computational meshes, a baseline adapted computational mesh with an estimated discretization-error of 0.1 counts is created from the initial fixed-complexity coarse computational mesh. This was done in 10 adaptive mesh refinement cycles using the error tolerance control feature. The initial drag for the adapted mesh was 471.30 counts with a mesh size of 16311 nodes. These 10 adaption cycles call the flow solver 1 time for each cycle, and these are included in the total number of flow solver calls for the design optimization problem.

Figure 4.17 illustrates the discretization-error adapted computational mesh that is the starting point for all adapted computational mesh cases in this research.

Figure 4.18 illustrates the computed Mach contours for the initial discretization-error adapted mesh, coarse fixed-complexity mesh, and fine fixed-complexity mesh, showing a more resolved shock on the adapted computational mesh compared to even the fine fixed-complexity computational mesh. Table 4.11 documents the fixed parameterization results for

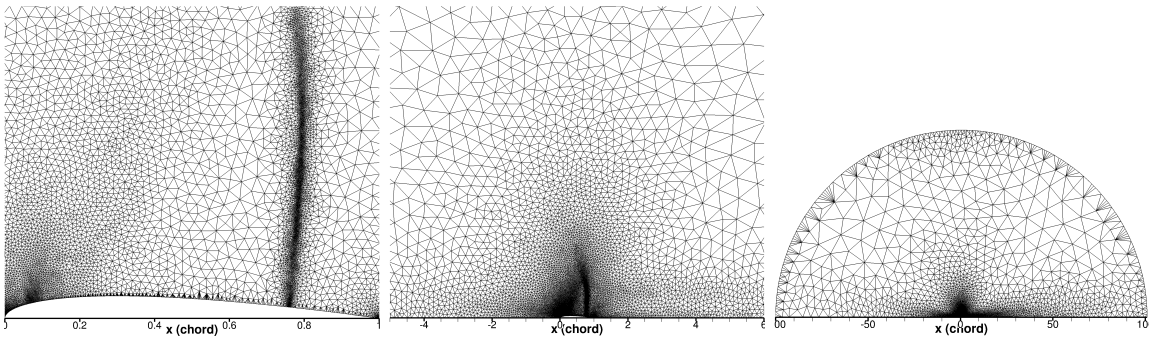

(a) Airfoil (b) Near Field (c) Far Field

Figure 4.17: Various views of the discretization-error adapted computational meshes

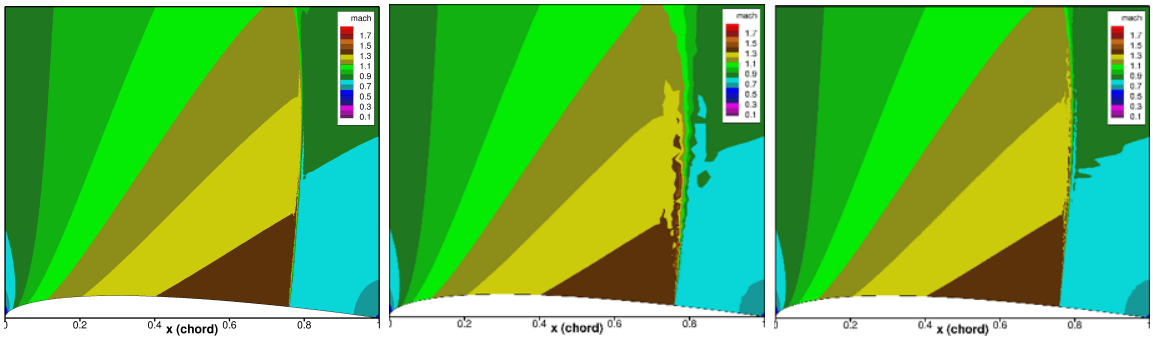

(a) Adapted (b) Coarse (c) Fine

Figure 4.18: Mach contour comparison of adapted and fixed-complexity computational meshes

the maximum allowable bounds discretization-error adapted computational meshes. These bounds range from 0.6 chord units for the 3 design-variable case to 0.02 for the 31 design-variable case. These bounds were determined by trail and error during the optimization process. The trial and error process began with setting very large bounds and then reducing the bounds until an optimization circuit could be completed. The 3 design-variable case for the adapted computational mesh required one less optimization circuit than the fixed-complexity computational mesh case. The adapted mesh reduced the drag to a value in between the fixed-complexity medium and fine computational mesh optimization cases, with fewer mesh points than the fixed-complexity coarse computational mesh. This decrease in

Table 4.11: Final design tabulated values for adapted mesh refinement case

Design Variables	Optimization Circuits	Flow Solver Calls (w/ AMR)	Mesh Size (nodes)	Objective Function: C_d	Optimality
3	3	75	30515	0.029178	1.9e-11
7	6	301	32072	0.013600	7.6e-9
15	4	278	36964	0.007478	1.6e-5
31	4	542	49591	0.004264	1.3e-7

mesh size creates a noticeable speedup in the design process. While the number of flow solver calls is approximately double that of the fixed-complexity computational mesh, this includes the mesh adaption flow solver calls. Ignoring the adaptation flow solver calls, the number is lower than the flow solver calls for the fixed-complexity computational mesh. While there is an increase in number of calls, the adapted mesh optimization cases require less wall-clock time than the optimization using the medium mesh at all optimization circuits, on a quarter of the required number of the computing cores. For the adaptive mesh refinement cases, no fixed bound cases were run. This is due to the ability of the max bound case to reduce the number of required optimization circuits to reach a converged solution. This need to reduce the number of optimization circuits is important for the adaptive mesh refinement cases, as the mesh must be readapted after each optimization circuit.

4.7 Adapted Mesh, Progressive Parameterization Results

An adapted mesh case for the progressive parameterization was performed to compare final solutions with the fixed complexity progressive parameterization. One of the measures of speed for this optimization research is the overall size of the mesh. This measure is used for this research, as the same computer hardware was not available for all the cases

performed in this study, which makes comparisons in terms of wall clock time infeasible. This is particularly important for the 31 design-variable case. During the optimization process, the "dove-tail" shape, seen also in the fixed mesh cases, begins to vanish and the trailing edge begins to round. In this case, the mesh will grow in complexity up to 200,000 mesh points, but then in the following optimization circuit and adaption, is able to drop back down in the 40-50,000 mesh point range. Figure 4.19 depicts an example mesh size growth during the adaption and optimization process. The mesh increases to approximately 160,000 nodes to resolve intermediate shocks that develop during the optimization and then decreases after the shocks are removed from the flow. The exception to this is the 31 design-variable

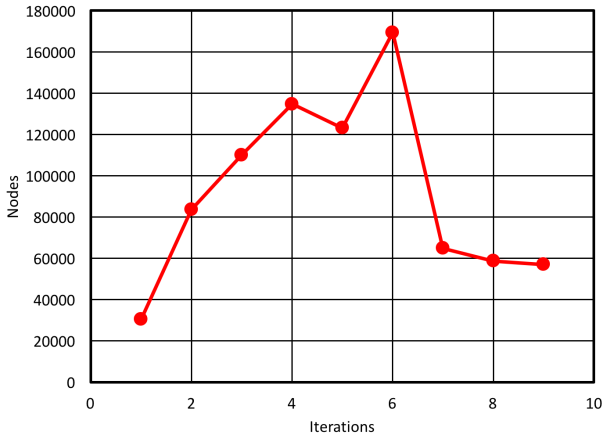

Figure 4.19: Example of adaptive mesh refinement mesh size growth

case, which saw mesh sizes over 1,000,000 nodes for an error estimate of 0.2 counts, which is double that of the desired value. With the option to coarsen the mesh, key flow features may be resolved while the mesh may return to a smaller size during the remainder of the design process. Table 4.12 documents the progressive parameterization results from the adapted mesh design problem. The results are similar for the first two design-variable cases with the fixed-complexity progressive parameterization cases. All completed results are within 3 to 5 counts of the fixed-complexity progressive parameterization drag values. The bounds for this case are the same as the fixed-complexity progressive optimization case. The 31

Table 4.12: Progressive design variable parameterization values for adapted mesh refinement case

Design Variables	Optimization circuits	Flow Solver Calls (w/ AMR)	Mesh Size (nodes)	Objective Function: C_d	Optimality
3	2	114	30515	0.029178	1.9e-11
7	2	155	30502	0.013944	5.2e-6
15	8	373	56998	0.007738	4.1e-8

design-variable case for the progressive parameterization was not completed, as the mesh grew too large to be adapted on the available resources for this research.

4.8 Adapted Mesh: Design followed by AMR

This research approaches coupling of the design optimization with adaptive mesh refinement in two ways, based on whether the error estimation occurs before or after shape optimization. Within FUN3D, the error estimation occurs during the adaption process. This means that for the design followed by adaptation approach, the error estimate occurs after the optimization. Alternatively, for the adaption followed by design approach, the error estimate occurs before the optimization. Figure A.3 illustrates the process for optimization-then-adaption and Figure A.4 the process of adaption-then-optimization. This study was performed to show that the order in which the optimization and mesh adaption occur does not impact the final solution. Micheletti [36] performed this same study using finite element methods for an advection-diffusion-reaction equation, finding that both methods reach the same solution. To demonstrate that the order in which the design and adaption is performed does not have an impact on the final design, a test was conducted with the 7 design-variable parameterization. Table 4.13 documents the results of the design followed by adaption method versus the adaption followed by design method for 7 design-variable. As seen in Table 4.13, the design then adaption mesh method was shown to reach the solution

Table 4.13: Adaption then optimization and optimization then adaption comparison

Method	Optimization circuits	Flow Solver Calls (w/ AMR)	Mesh Size (nodes)	Objective Function: C_d	Optimality
AMR then Design	6	301	32072	0.013600	7.6e-9
Design then AMR	4	172	35198	0.013680	1.7e-5

in fewer optimization circuits, but the final drag values are almost identical in both design cases. The final airfoil shapes are also almost identical between the two methods as well.

4.9 Progressive, Fixed-Computational Mesh Refinement

This is a method of improving the design by starting on a coarse fixed-complexity computational mesh and then moving to the next finer fixed-computational mesh to further improve the design. This transfer to the next computational mesh can be performed with two different parameterizations. In the first case, the same parameterization as the coarser mesh is used on the next finer mesh. In the second case the parameterization is refined as the shape is applied to the next finer mesh. For each increase in mesh refinement, the final design variables are applied to the next mesh. These are applied from the original airfoil and the shape is updated by inputting the design variable values obtained from the previous optimization. All shapes are moved to the next mesh after one optimization circuit.

4.9.1 Fixed Design Variable Parameterization

Starting with the coarse fixed-complexity computational mesh and 3 design variables, the design shape changes obtained on the coarse mesh are applied to the medium fixed-complexity computational mesh. For the medium mesh, the maximum additional shape

Table 4.14: 3 design-variable progressive mesh design optimization

Mesh	Optimization Circuits	Flow Solver Calls	Objective Function: C_d	Optimality	Optimization Complexity Function
Coarse	1	21	0.029247	1.7e-5	0.08748
Medium	1	22	0.029193	2.6e-8	0.17845
Fine	1 (3)	11 (54)	0.029151	2.0e-6	0.25225
Fine - Fixed	4	78	0.029152	7.7e-10	1.34354

Table 4.15: 7 design-variable progressive mesh design optimization

Mesh	Optimization Circuits	Flow Solver Calls	Objective Function: C_d	Optimality	Optimization Complexity Function
Coarse	1	72	0.013621	4.3e-7	0.03513
Medium	1	52	0.013604	2.6e-6	0.05958
Fine	1 (3)	41 (165)	0.013598	3.7e-6	0.10597
Fine - Fixed	7	277	0.013598	1.2e-8	0.72874

changes produced by the optimizer on the medium mesh were 1.54E-4 chord units. This is a minor change and resulted in a change in drag of 0.3 counts of drag. This was repeated for the fine fixed-complexity computational mesh. The results for the 3 design variable case are documented in Table 4.14, while the results for the 7 design variable are shown inTable 4.15.

This method showed that the same final shape and drag value results are reached with fewer flow solver calls than performing the optimization on the fine mesh only. The bounds for the coarse mesh were set to the maximum allowable for proper mesh convergence, 0.1. The bounds for the medium mesh and fine mesh were set to 0.028. With the larger bounds applied to the coarse mesh, the majority of the design was performed at a lower computational cost by using the coarse mesh. This also resulted in fewer optimization circuits and fewer total flow solver calls during the optimization process. For the 7 design-variable case in particular,

Table 4.16: Progressive parameterization with progressive mesh design optimization

Mesh	Optimization Circuits	Flow Solver Calls	Objective Function: C_d	Optimality	Optimization Complexity Function
Coarse	1	21	0.029247	1.7e-5	0.08748
Medium	1 (2)	41 (62)	0.013635	1.1e-6	0.05314
Medium - Fixed	7	269	0.013606	1.5e-6	0.35861
Fine	1 (3)	33 (95)	0.012148	2.3e-7	0.07588

the total number of optimization circuits was reduced from 7 to 3, cutting the user interaction by more than half. The total number of flow solver calls was reduced by over 100, with only 41 being required for the fine mesh, greatly reducing the computational time to converge the solution. This is also reflected in the O.C.F., with the sum of this process being less than the O.C.F. of the fine mesh only optimization.

4.9.2 Progressive Design Variable Parameterization

In this approach, optimization is performed on progressively finer meshes, similarly to the previous case with the addition of progressive design-variable parameterization. Starting on the coarse mesh with three design variables, the mesh level is increased to the medium mesh with 7 design variables. To perform this, the medium mesh must first be adjusted with the final 3 design-variable shape changes and then reparameterized with 7 design-variable shape. Table 4.16 documents these results. This same process is repeated using 15 design variables on the fine mesh for the final design.

This method was able to further reduce the objective function and allowed for optimization to be performed on the fine mesh with 15 design variables, which was previously deemed too expensive with the given number of optimization circuits required for the 15 design-variable case. The medium mesh was able to reach the same solution as the 7 design-variable values from the fixed parameterization work, in a quarter of the flow solver calls

and in 2 optimization circuits, compared to that required previously. In a total of 95 flow solver calls, this process was able to reduce the drag of the airfoil by 330 counts, which was the most efficient of all the methods used in this research. An extension of this would be to take this same method and move to mesh adaption, by performing preliminary designs on a mesh with a larger error tolerance and as the parameterization is increased, the error tolerance could be tightened.

Chapter 5

Results for Test Case 2: Transonic, RANS, Lift Penalized, Drag Minimization

Test case 2 uses the TMA-0712 airfoil that was created in the Flow Physics and Control branch at NASA Langley by Lewis Owens and William Milholen [46]. This optimization routine minimizes the viscous and pressure drag while maintaining a target coefficient of lift of 0.7. This airfoil is one that has already been optimized using CDISC [47], a pressure coefficient inverse design method. This research looks to improve upon this design with the use of adjoint methods.

5.1 Problem Description

The airfoil is placed into Pointwise from a data file of points provided by Lewis Owens [48]. The trailing edge is blunt with a thickness of 0.006 chord units. All computations are performed on a full mesh with a stretched, anisotropic mesh in the viscous sublayer

region that wraps around the airfoil, similar to an O-mesh. There is no wake for the fixed-complexity computational meshes in order to keep the computational meshes more uniform within the family.

5.2 Solver Setup

This research uses the following non-default FUN3D settings to converge the problem:

- Compressible, turbulent, viscous flow equations
- Mach 0.78
- Reynolds Number 30 million
- Objective function L = $C_d^2 + (C_l - 0.7)^2$
- Van Leer flux vector splitting is used for both the residual and Jacobian inviscid flux construction. This was done for consistency with the first test case. While this is typically viewed as a poor flux construction method for viscous flows, convergence is generally more robust using this choice.
- Residual stopping criteria of 1E-13 for the flow, and adjoint solvers to ensure that the Hessian is accurately approximated as possible within SNOPT
- Mesh movement residual stopping criteria of 1E-13 for the mesh movement equations to reduce the likelihood of negative volumes. By reducing the likelihood of negative volumes, the bounds may be larger which results in a lower number of optimization circuits.
- SNOPT Optimality stopping criteria is set to 1E-40 to ensure a full converged design problem without an early exit. This is a hard-coded limit in FUN3D. It must be

hardcoded as there is a bug within SNOPT that does not allow it to read in an optimality tolerance from an input file.

- A maximum of 1000 Krylov Vectors are used for the flow solver and adjoint solver. This is not a default option for FUN3D, but it allows for increased CFL ramping and consistent convergence for every flow solver and adjoint solver evaluation. By using this large number of Krylov vectors, memory becomes an issue for the adjoint solver in particular, so this method may not be appropriate for larger, 3D cases.

These solver settings help expedite the residual convergence and design optimization process. These were determined beforehand with initial testing of the design cases.

5.3 Fixed-Complexity Computational Mesh Generation

A family of meshes is created with target node counts for each level using Pointwise. Table 5.1 details the settings used in Pointwise to create the meshes. These use the collared mesh approach detailed in Chapter 2. The boundary decay feature within Pointwise, a value that varies from 0 to 1, controls how quickly the cells grow as the advancing front of the computational mesh approaches the boundaries. A higher value corresponds to less growth. The airfoil spacing refers to the node spacing on the airfoil, using a unit chord airfoil and the spacing being the respective fraction of the chord.

Table 5.1: Pointwise settings for Test Case 2

Mesh	Boundary Decay	Airfoil Spacing	Node Count	Viscous Layers	y+	Growth Rate
Coarse	0.5	0.004	45819	40	3	1.2
Medium	0.982	0.002	101520	40	1.5	1.2
Fine	0.99815	0.001	300,782	39	1	1.2

Table 5.1 gives the quantities for the controllable features within Pointwise used to create

the family of fixed-complexity computational meshes. These settings, in combination with the collared mesh approach, can be used to recreate these meshes.

5.4 Fixed-Complexity Computational Mesh, Fixed Parameterization Results

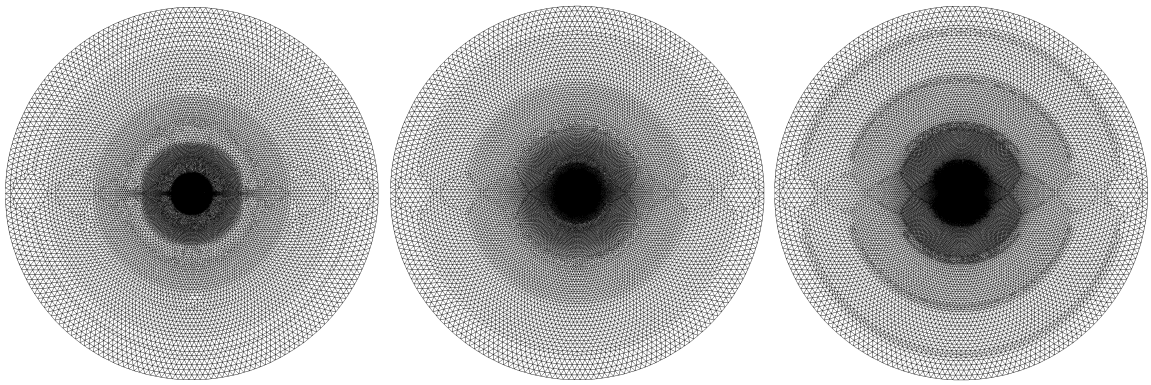

(a) Coarse (b) Medium (c) Fine

Figure 5.1: Overall view of fixed-complexity computational meshes

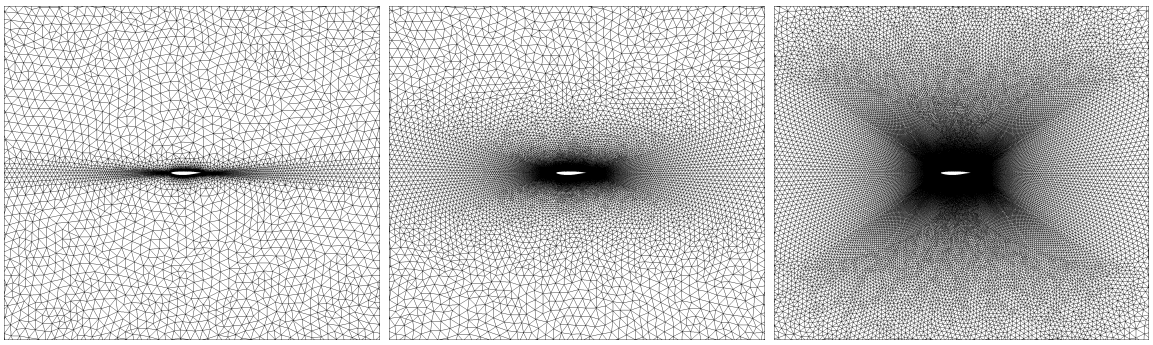

(a) Coarse (b) Medium (c) Fine

Figure 5.2: Zoomed view of fixed-complexity computational meshes

Figures 5.1 through 5.4 depict the family of fixed-complexity computational meshes and allow for visualization of the collaring effects.

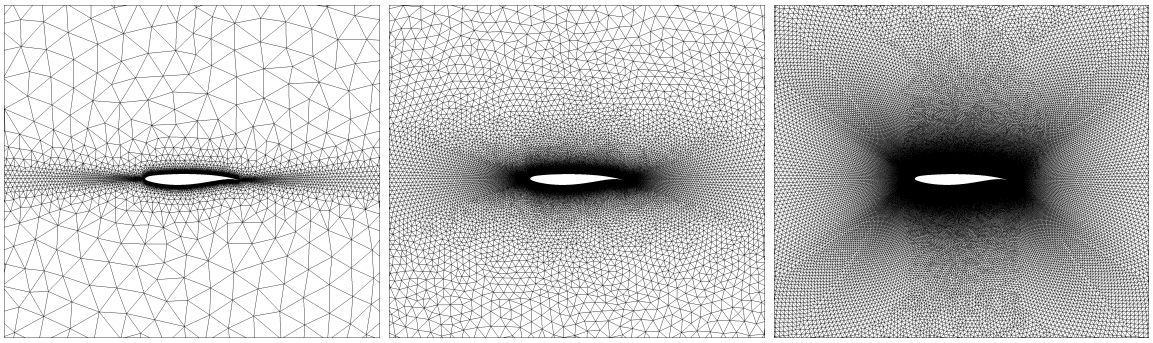

(a) Coarse (b) Medium (c) Fine

Figure 5.3: Near-field view of fixed-complexity computational meshes

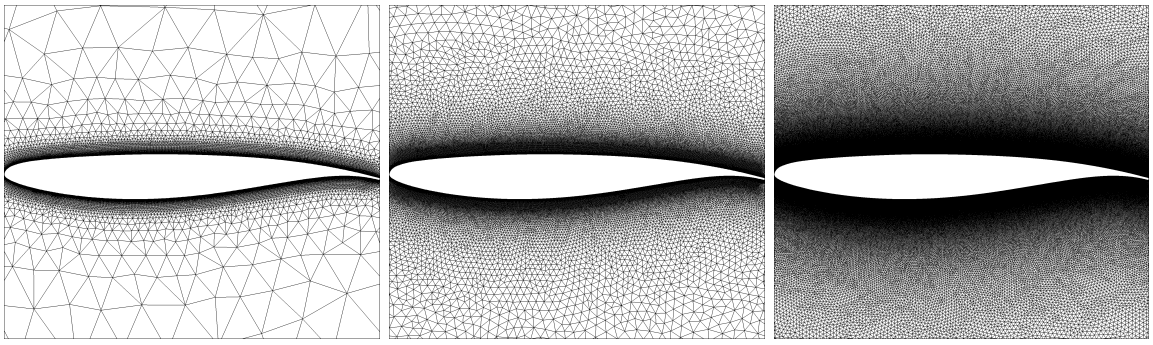

(a) Coarse (b) Medium (c) Fine

Figure 5.4: Airfoil view of fixed-complexity computational meshes

A computational mesh convergence study is performed to determine the reference baseline lift value for the TMA-0712 airfoil. Figure 5.5 is the lift convergence plot for the family of fixed-complexity computational meshes. The computed coefficient of lift of the nominal airfoil on the fine fixed-complexity computational mesh is 0.6890. Extending this plot to the y-intercept (1/nodes = 0) gives the infinite resolution coefficient of lift value of 0.7234, which is within 5% of the C_l value of the finest mesh. These values bracket the target C_l value of this airfoil, which is 0.7.

Figure 5.6 depicts the Mach contours for the coarse, medium, and fine fixed-complexity computational meshes, showing as the mesh is refined, the shock resolution becomes sharper. Figure 5.7 shows the computed surface pressure coefficient for the family of fixed-complexity

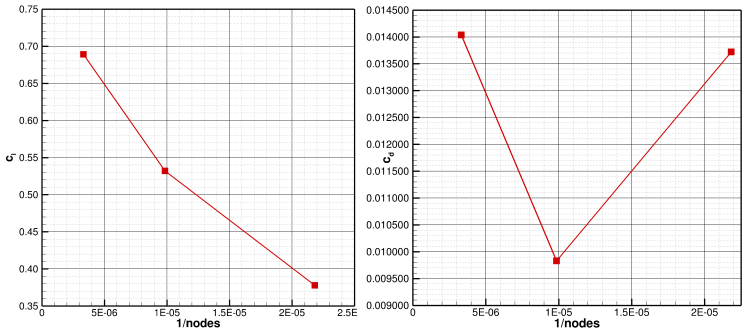

(a) Lift (b) Drag

Figure 5.5: Lift and drag convergence for the fixed-complexity computational mesh on the initial shape of the TMA-0712

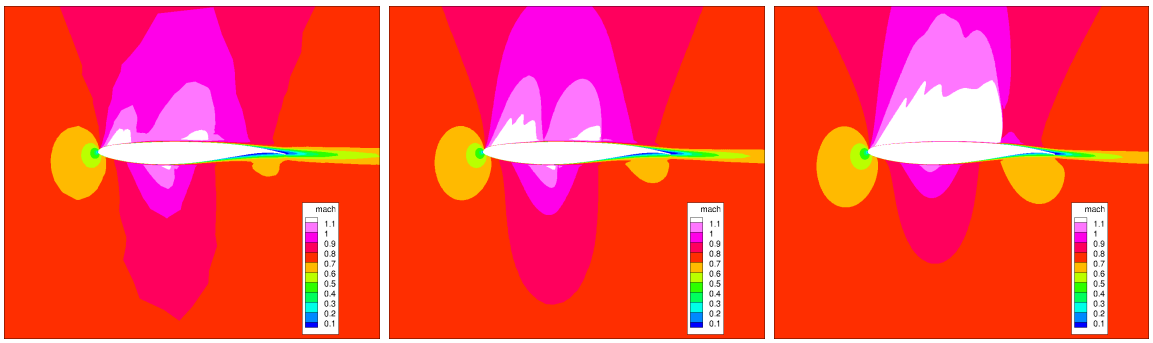

(a) Coarse (b) Medium (c) Fine

Figure 5.6: Mach convergence for the family of fixed-complexity computational meshes

computational meshes. The shock occurs at approximately the 0.75 chord location. As the resolution of the mesh increases, the shock becomes sharper. Throughout this design problem, the overall goal is to reduce the shock strength while maintaining the target lift of 0.7 for every mesh. During this exercise, it is seen that the coarse and medium meshes do not have the required resolution for producing an accurate solution of the flow over this airfoil. Additional evidence is provided by the example design result from the coarse mesh with 31 design variables seen in Figure 5.8. This illustrates that the optimization process is highly influenced by the discretization-error, as an under-resolved computational mesh is unable to provide accurate sensitivities for the optimizer. The resulting shapes are then impractical

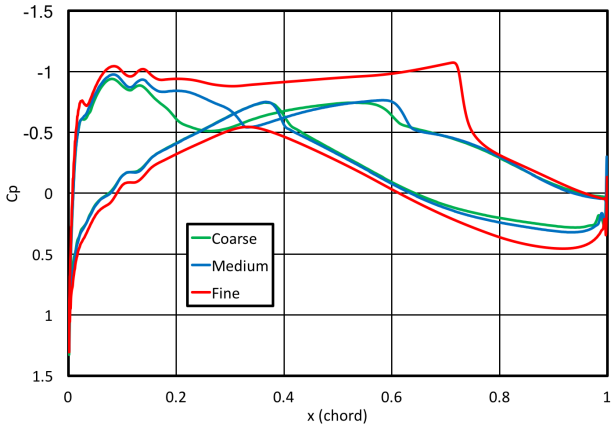

Figure 5.7: Surface coefficient of pressure profiles for the family of meshes

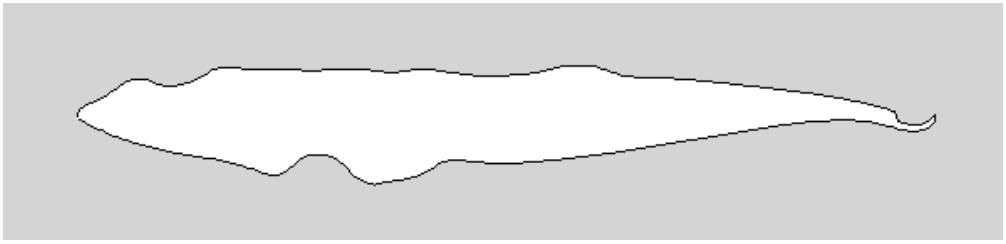

Figure 5.8: Example of design result from under-resolved computational mesh

for design and testing. The fine mesh appears to have the proper resolution, leading this to be considered as the only suitable mesh for future research.

5.5 Fixed-Complexity Computational Mesh, Fixed Parameterization Results

5.5.1 Seven Design-Variables

For the 7 design-variable case, and for all the fixed parameterization cases, the optimization process started with the TMA-0712 airfoil, and the optimization was run until the output values leveled off at a final design value on the fine mesh only.

Table 5.2: 7 design-variable final design tabulated values for the fine mesh

Optimization Circuits	Flow Solver Calls	Objective Function	C_l	C_d	Optimality
10	1313	0.0006257	0.6994	0.007908	2.2e-6

Table 5.3: Progressive parameterization final design tabulated values for the fine mesh

Design Variables	Optimization Circuits	Flow Solver Calls	Objective Function	C_l	C_d	Optimality
7	10	1313	0.0006257	0.6994	0.007908	2.2e-6
15	1	19	0.0006247	0.7000	0.007904	9.1e-5

Table 5.2 documents the final totals from the 7 design-variables design problem for the fine mesh. The drag was reduced by 55 counts and the lift was increased from 0.6890 to 0.6994.

5.6 Fixed-Complexity Computational Mesh, Progressive Parameterization Results

Table 5.3 details the final totals of the progressive parameterization results for the fine fixed-complexity computational mesh. Seven design-variables were used as the initial starting shape. Minor improvements were made to both the lift and drag, with lift reaching the target goal.

Figure 5.9 depicts the surface C_p profiles for the initial shape, the 7 design-variable optimized surface, and the final 15 design-variable surface. The shock strength is significantly reduced, allowing for the reduction in drag.

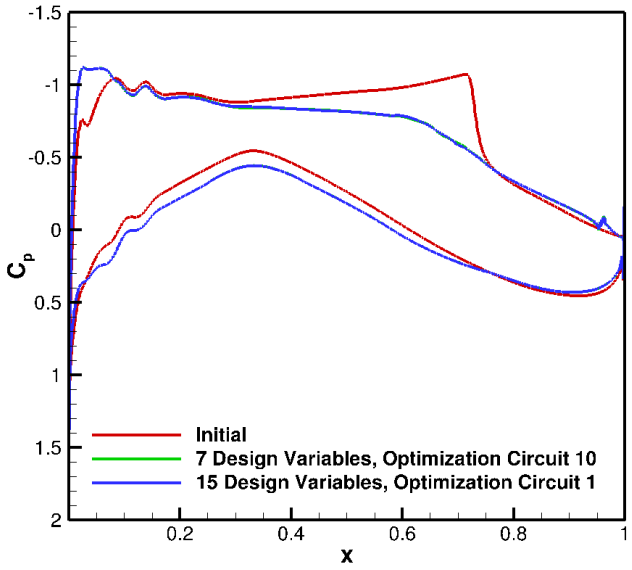

Figure 5.9: Initial and final C_p profiles for 7 and 15 design variables

5.7 Adaptive Mesh Refinement

Initially, the test case was attempted using isotropic cells for the mesh adaption. It was found that this would lead to a cell volume of 5e-13 for the first cell for a y+ value of 1 and a total number of surface mesh points of over 2 million. This mesh size is impractical for the application of most CFD codes. Since this research was restricted to the use of isotropic cell adaption, mesh adaption was not possible for this test case. There have been preliminary attempts during this research of the application of anisotropic adaptive meshes with cell aspect ratios of up to 100,000. While this is rather high, it does allow for much better resolution of the boundary layer and the wake, with fewer cells. This appears to be promising, as the mesh size is much closer to the size of the fine mesh for this research, which is undersized as there is no wake for fine mesh and the y+ value of 1 is considered the upper limit required for proper boundary layer resolution.

Chapter 6

Conclusions and Lessons Learned

6.1 Conclusions for Test Case 1

The current practice of using fixed-complexity computational meshes was found to be more time efficient during the design process and to incur a lower user interaction penalty compared to the use of loosely coupled AMR and optimization. This is true for the methods employed in this research. The user interaction occurs through the toolbox setup within FUN3D and could be reduced with scripting, but there will still be many more flow solver calls with an adapted mesh refinement technique compared to the fixed-complexity computational mesh approach. This is due to the need to readapt the mesh at the end of each optimization circuit. Readaption is required as the shape change may cause the discretization-error to increase in the mesh. A possible way to reduce this would be to use smaller bounds so that the shape does not change as rapidly. This is not a typical case though, as most design problems for real-world simulations will be starting from an already preliminary optimized shape, therefore the changes will typically be inherently small. Additionally, the error estimates provided in the mesh refinement process may be used to help with the ever increasing desire to apply statistical bounds to the solutions. This will help with certainty

in the final design before performing wind-tunnel testing and flight testing. One issue that arose during this work for the adapted meshes is that the meshes tend to grow rapidly in size when there are dramatic shape changes. One solution to alleviate this has been to try smaller bounds. Meshes were observed to increase by an order of magnitude or more in size in the presence of large shape changes, which adversely impacted the efficiency of the process. It may be more efficient to perform many optimization circuits with smaller changes to the design to help keep the mesh size down. An additional alternative method to maintain smaller meshes sizes would be to perform progressive error tolerance with the loosely coupled AMR approach.

6.2 Conclusions for Test Case 2

After the difficulties with the adaptive mesh refinement, and the under resolved coarse and medium fixed-complexity computational meshes, this test case focused on documenting and determining the best starting point for a previously optimized airfoil. A previously optimized airfoil may be started with a relatively refined parameterization and achieve much improvement for a relatively low cost. The shock is able to be reduced, which in turn reduces the overall drag of the shape. However, one potential issue for transonic flight is the creation of a single point-design airfoil that may be very ill-performing for other conditions. To determine this, the shape should be tested at these other conditions and potentially designed using multi-point optimization.

6.3 General Conclusions

Included are some general observations and conclusions from this research. The first is that an increase in design-variables leads to a more optimal final shape. The second is that

the number of required flow solver calls increases with the number of design-variables and with mesh complexity. Thirdly, it was found that bound settings can dramatically impact the total cost. Too large bound settings may cause oscillations in the final shape, prolonging the design process. Too small bound settings may require multiple reparameterizations during the design process. Fourth, progressive parameterizations may reduce the number of flow solver calls and the overall cost of the optimization. Fifth, progressive mesh complexity reduces the number of flow solver calls and opens design optimization possibilities on the more refined meshes that may have previously been deemed infeasible. A combination of progressive mesh complexity and progressive parameterization leads to an even larger cost reduction. Finally, AMR with design optimization reduces cost through mesh complexity reduction, but there are cost increases due to the additional flow solver calls for the AMR and the user interaction is doubled for each optimization circuit due to the current FUN3D workflow.

6.4 Operational Lessons Learned

6.4.1 Fully converging the flow solution and adjoint solution

One of the most critical lessons learned from this research is that the flow solution and adjoint solution must be fully converged for consistent optimization results. Fully converged solutions enable the optimizer to better approximate the Hessian for the optimization. If this is not done, the optimization tends to oscillate, and the optimizer will exit after reporting numerical difficulties. To ensure the flow solver can converge more fully at each step, the bounds must also be tightened on the design variables for the optimizer. Tightened bounds limit the ability of the shape to change, therefore avoiding the introduction of shape changes that disrupt the flow and in turn make the solution more amenable to convergence. Figure 6.1 illustrates a case when the flow solution does not achieve convergence. The output solution

for the adjoint and for the optimizer is now dictated by where the solution is stopped within this unsteady behavior. The effect of tightening the bounds on the design space has not been completely determined, and is recommended for future work.

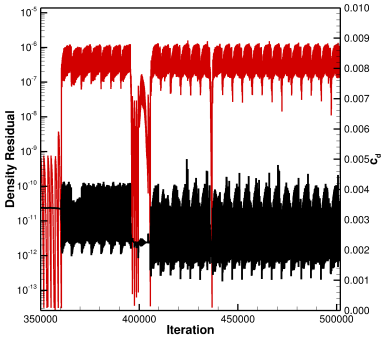

Figure 6.1: Unconverged residuals

6.4.2 Fully converging mesh movement problem

One of the early limiting factors on the inflation of the bounds was the development of negative cell volumes during mesh movement. Fully converging the mesh movement problem to machine zero helped remove many of the negative cell volumes that arose during large shape changes. By doing this, the optimization can perform the changes with fewer optimization circuits. Potentially the same solution can be reached with the smaller bounds, but this requires many more optimization circuits and increases the time dramatically.

6.4.3 Tightening bounds

Like the flow solution problem above, occasionally the design-variable value will oscillate within the bound limits during an optimization circuit. This causes the optimizer to constantly adjust the design-variable, never converging to a solution, until it hits the major iteration limits prescribed by the user. For example, during this research one particular case called the flow solver over 1500 times and the optimizer was only adjusting the thickness

of the shape by 1e-4 or less. Since the optimizer could make the changes and there was a difference in the solution, the optimizer continued to try to improve the design until the major iteration limit was reached. Slightly tightening the bounds can remove this behavior, and the design optimizer can converge to a solution in more than order of magnitude or fewer flow solver calls. Figure 6.2 gives a comparison on the same starting point of an airfoil. The loose bounds condition had bounds of 0.01 and the tight bounds test had bounds of 0.005. Halving the bounds reduced the number of flow solutions by over 1400, while producing the same final answer of 0.003621. This is different from the problem of not fully converging the flow solver; these are both fully converged within the flow solver, but when the optimizer slightly adjusts the shape, the overall optimization problem cannot converge.

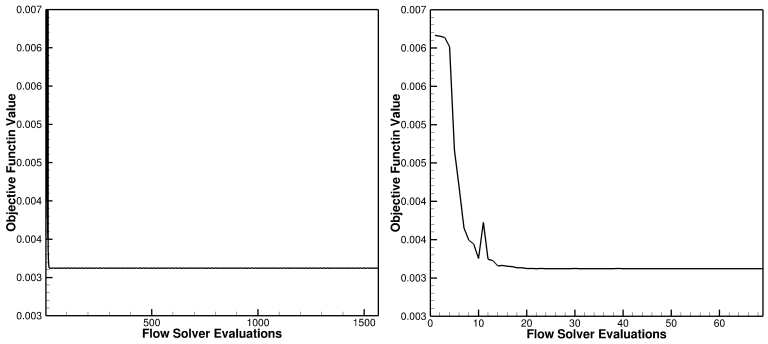

(a) Loose bounds (b) Tight bounds

Figure 6.2: Bound limit comparison

6.4.4 Isotropic Mesh Adaption

Since the adapted meshes for this thesis are limited to isotropic cells, the adaption presented is infeasible for a viscous flow case due to the computational tools used. FUN3D has anisotropic mesh adaption capabilities but these were not used for this research. The main limiting factor is the adaption toolbox itself. It is still a serial mesh adaption tool, which means that memory overhead is an issue. The memory overhead due to the required

number of surface nodes to resolve the boundary layer and maintain isotropic cells exceeds the ability to continue calculations. In future work, invoking the anisotropic adaptive mesh refinement capability within FUN3D should enable this work to become feasible for 2D viscous flow problems.

6.4.5 Restart vs Uniform start for design problems

All cases in the research presented here were performed with restarts between each reparameterization. The initial restart is generated by running FUN3D's flow solver and saving the restart file, which is flagged to be saved within the input namelist. A new restart file is saved at the end of each optimization cycle within an optimization circuit and used as the initial conditions for the next optimization cycle. Restarts between parameterizations are achieved by modifying FUN3D to read in a restart file each time. Restarts were not used during the progressive fixed-complexity mesh research, as the meshes were increasing in size and the flow solution was not able to be interpolated onto the new finer mesh. Restarts were used during the adaption process by starting the process from the second cycle, which uses the restart from the previous iteration during the adaption process. This allowed for a single continuous restart file chain during the adaption process. This change was made after early work showed a discrepancy between the final solution, obtained using a restart file and the solution obtained starting with uniform flow initial conditions for the reparameterized geometry. This difference was seen because the solution initialized with uniform flow was not always able to reach a machine precision converged solution after a reparameterization. More work needs to be done in this area, as both cases should provide the same solution, whether starting from a restart or uniform flow initial conditions.

6.4.6 Bound Limits on Adapted Meshes

As mentioned in the conclusions to the first test case, future work should include research concerning the magnitude of bounds allowed for adaptive meshing cases. This is recommended as a result of the observation that some cases led to the generation of very large meshes based on the specified error criteria when large shape changes were requested by the optimizer.

6.5 Recommendations for Future Work

From this research, adaptive mesh refinement appears to provide a way to improve upon design optimization cases for final values. While it may be more computationally expensive currently with the large amount of user interaction required for performing adaptive mesh refinement and design optimization within the FUN3D framework, developments can be made to reduce this interaction and automate much of these processes. A progressive AMR error tolerance is recommended for future work to determine if there are potential benefits, similar to the benefits observed in the progressive mesh complexity cases performed in this work

Future work recommendations include the use of anisotropic cells in the mesh refinement process. This will allow for even further reduced mesh sizes. A potential issue with highly stretched cells can be that smaller bounds may be required to prevent the occurrence of negative volumes. Another recommendation is to incorporate global optimization schemes into the initial design optimization process to help narrow the design space, after which local optimization schemes may be used to finish optimizing the shape. As the adapted meshes provide the user with error estimates, these estimates may be useful for uncertainty quantification (UQ) during the design process. UQ is becoming an ever increasing desire for design optimization as it allows for realistic bounds to be placed on values, helping to

improve the certainty of the design before production begins. Moving the adaption and design optimization to three-dimensional problems is also recommended moving forward, allowing for more true and realistic shapes to be developed for both wind tunnel testing and flight testing.

Appendix A

Numerical Approach Figures

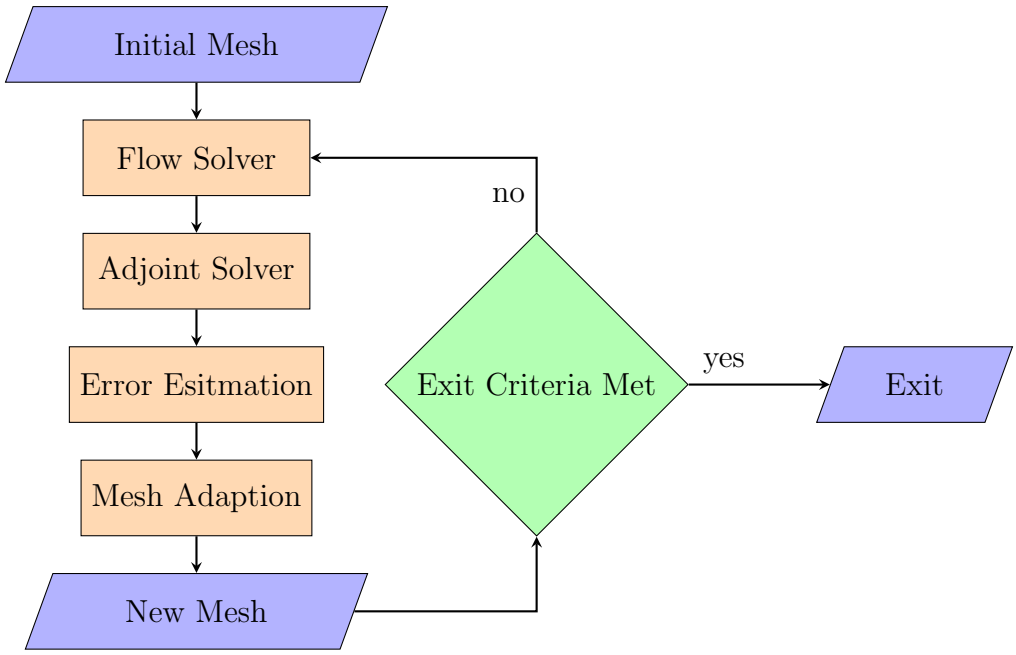

Figure A.1: Computational mesh adaption process within FUN3D

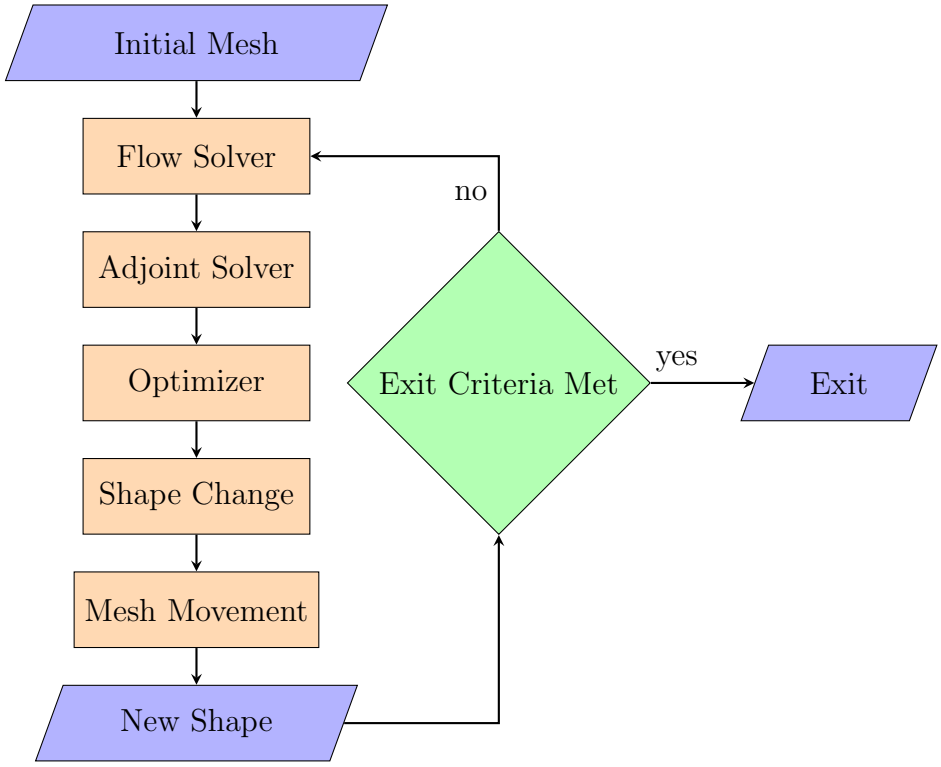

Figure A.2: Design optimization process within FUN3D

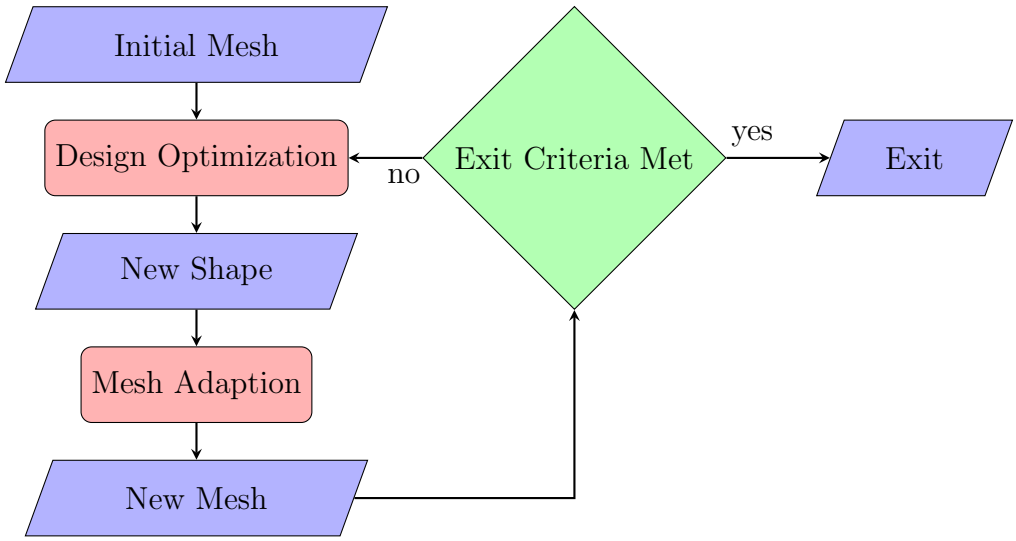

Figure A.3: Optimization then adaptation

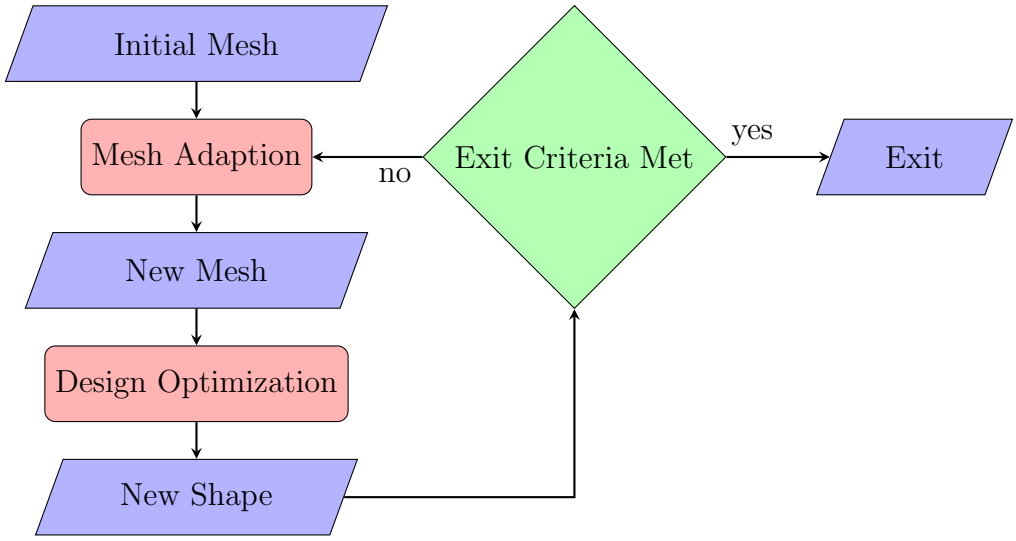

Figure A.4: Adaption then optimization

Bibliography

[1] Li, D. and Hartmann, R., "Adjoint-Based Error Estimation and Mesh Refinement in an Adjoint-Based Airfoil Shape Optimization of a Transonic Benchmark Problem," *Notes on Numerical Fluid Mechanics and Multidisciplinary Design*, Vol. 132, 2016, pp. 537–546.

[2] "AIAA Aerodynamic Design Optimization Discussion Group," https://info.aiaa.org/tac/ASG/APATC/AeroDesignOpt-DG/default.aspx.

[3] Anderson, G. R., Nemec, M., and Aftosmis, M. J., "Aerodynamic Shape Optimization Benchmarks with Error Control and Automatic Parameterization," AIAA 2015-1719, 53rd AIAA Aerospace Sciences Meeting, Kissimmee, FL January 2015.

[4] "CART3D Software," https://www.nas.nasa.gov/publications/software/docs/cart3d/pages/cart3Dhome.html.

[5] Park, M. A., *Anisotropic Output-Based Adaptation with Tetrahedral Cut Cells for Compressible Flows*, Ph.D. thesis, Massachusetts Institute of Technology, September 2008.

[6] Jameson, A., "CFD for Aerodyanmic Design and Optimization: Its Evolution over the Last Three Decades," AIAA 2003-3438, 16th AIAA Computational Fluid Dynamics Conference, Orlando, FL June 2003.

[7] Jameson, A., "Efficient Aerodyanmic Shape Optimization," AIAA 2004-4369, 10th AIAA/ISSMO Multidisciplinary Analysis and Optimization Conference, Albany, NY August 2004.

[8] Vassberg, J. C. and Jameson, A., "Aerodynamic Shape Optimization Part I: Theortical Background," Lecture 1, Von Karman Institute, 2006.

[9] Vassberg, J. C. and Jameson, A., "Industrial Applications of Aerodynamic Shape Optimization," Lecture 2, Von Karman Institute, 2014.

[10] Mavriplis, D. J., "A Discrete Adjoint-Based Approach for Optimization Problems on Three-Dimensional Unstructured Meshes," AIAA 2006-0050, 44th AIAA Aerospace Sciences Meeting and Exhibit, Reno, NV January 2006.

[11] Poole, D., Allen, C., and Rendall, T., "A Constrained Global Optimization Framework," AIAA 2014-2034, 14th AIAA Aviation Technology, Integration, and Operations Conference, Atlanta, GA June 2014.

[12] Poole, D., Allen, C., and Rendall, T., "Comparison of Local and Global Constrained Aerodynamic Shape Optimization," AIAA 2014-3223, 32nd AIAA Applied Aerodynamics Conference, Atlanta, GA June 2014.

[13] Buckley, H. P., Zhou, B. Y., and Zingg, D. W., "Airfoil Optimization Using Practical Aerodynamic Design Requirements," *Journal of Aircraft*, Vol. 47, No. 5, September-October 2010, pp. 1707–1719.

[14] Samareh, J. A., "Survey of Shape Parameterization Techniques for High-Fidelity Multidisciplinary Shape Optimization," *AIAA Journal*, Vol. 39, No. 5, 2001, pp. 877–884.

[15] Vassberg, J. C. and Jameson, A., "Influence of Shape Parameterization on Aerodynamic Shape Optimization," Lecture 3, Von Karman Institute, 2014.

[16] Samareh, J., "Multidisciplinary aerodynamic-structural shape optimization using deformation (MASSOUD)," AIAA 2000-4911, 8th Symposium on Multidisciplinary Analysis and Optimization, Long Beach, CA September 2000.

[17] Castonguay, P. and Nadarajah, S. K., "Effect of Shape Parameterization on Aerodynamic Shape Optimization," AIAA 2007-59, 45th AIAA Aerospace Sciences Meeting and Exhibit, Reno, NV January 2007.

[18] Mousavi, A., Castonguay, P., and Nadarajah, S. K., "Survey of Shape Parameterization Techniques and its Effect on Three-Dimnesional Aerodynamic Shape Optimization," AIAA 2007-3837, 18th AIAA Computational Fluid Dynamics Conference, Miami, FL June 2007.

[19] Anderson, G., Aftosmis, M., and Nemec, M., "Parametric Deformation of Discrete Geometry for Aerodynamic Shape Design," AIAA 2012-0965, 50th AIAA Aerospace Sciences Meeting including the New Horizons Forum and Aerospace Exposition, Nashville, TN, January 2012.

[20] "Blender," https://www.blender.org.

[21] Anderson, G. R. and Aftosmis, M. J., "Adaptive Shape Control for Aerodynamic Design," NAS NAS-2015-02, NASA Ames Research Center, 2015.

[22] Park, M. A., Krakos, J. A., Michal, T., Loseille, A., and Alonso, J. J., "Unstructured Grid Adaption: Status, Potential Impacts, and Recommended Investments Toward CFD Vision 2030," AIAA 2016-3323, 46th AIAA Fluid Dynamics Conference, Washington, DC June 2016.

[23] Slotnick, J., Khodadoust, A., Alonso, J., Darmofal, D., Gropp, W., Lurie, E., and Mavriplis, D., "CFD Vision 2030 Study: A Path to Revolutionary Computational Aerosciences," NASA-CR-218178, March 2014.

[24] Venditti, D. A. and Darmofal, D. L., "Grid Adaption for Functional Outputs: Application to Two-Dimensional Inviscid Flows," *Journal of Computational Physcis*, Vol. 176, 2002, pp. 40–69.

[25] Venditti, D. A. and Darmofal, D. L., "Anisotropic grid adaptation for functional outputs: application to two-dimensional viscous flows," *Journal of Computational Physcis*, Vol. 187, February 2003, pp. 22–46.

[26] Nemec, M. and Aftosmis, M. J., "Output Error Estimates and Mesh Refinement in Aerodyanmic Shape Optimization," AIAA 2013-865, 51st AIAA Aerospace Sciences Meeting including the New Horizons Forum and Aerospace Exposition, Dallas, TX January 2013.

[27] Dalle, D. J. and Fidkowski, K. J., "Multifidelity Airfoil Shape Oprimization Using Adaptive Meshing," AIAA 2014-2996, 32nd AIAA Applied Aerodynamics Conference, AIAA AVIATION Forum, Atlanta, GA June 2014.

[28] Heath, C. M., Gray, J. S., Park, M. A., Nielsen, E. J., and Carlson, J.-R., "Aerodynamic Shape Optimization of a Dual-Stream Supersonic Plug Nozzle," AIAA 2015-1047, 53rd AIAA Aerospace Sciences Meeting, Kissimmee, FL January 2015.

[29] Becker, R., Kapp, H., and Rannacher, R., "Adaptive Finite Element Methods for Optimal Control of Partial Differential Equations: Basic Concept," *SIAM Journal on Control and Optimization*, Vol. 39, No. 1, 2000, pp. 113–132.

[30] Becker, R. and Rannacher, R., "An optimal control approach to a posteriori error estimation in finite element methods," *Acta Numerica*, Vol. 10, 5 2001, pp. 1–102.

[31] Becker, R., "Mesh Adaption for Stationary Flow Control," *Journal of Mathematical Fluid Mechanics*, Vol. 3, 2001, pp. 317–341.

[32] Becker, R. and Vexler, B., "Optimal control of the convection-diffusion equation using stabilized finite element methods," *Numerische Mathematik*, Vol. 106, No. 3, 2007, pp. 349–367.

[33] Dede', Luca, Q. and Alfio, "Optimal control and numerical adaptivity for advection–diffusion equations," *ESAIM: Mathematical Modelling and Numerical Analysis - Modélisation Mathématique et Analyse Numérique*, Vol. 39, No. 5, 2005, pp. 1019–1040.

[34] Hintermüller, M. and Hoppe, R. H. W., "Goal-Oriented Adaptivity in Control Constrained Optimal Control of Partial Differential Equations," *SIAM Journal on Control and Optimization*, Vol. 47, No. 4, 2008, pp. 1721–1743.

[35] Li, R., Liu, W., Ma, H., and Tang, T., "Adaptive Finite Element Approximation for Distributed Elliptic Optimal Control Problems," *SIAM Journal on Control and Optimization*, Vol. 41, No. 5, 2002, pp. 1321–1349.

[36] Micheletti, S. and Perotto, S., "The Effect of Anisotropic Mesh Adaptation on PDE-Constrained Optimal Control Problems," *SIAM Journal on Control and Optimization*, Vol. 49, No. 4, 2011, pp. 1793–1828.

[37] Yan, N. and Zhou, Z., "A priori and a posteriori error analysis of edge stabilization Galerkin method for the optimal control problem governed by convection-dominated diffusion equation," *Journal of Computational and Applied Mathematics*, Vol. 223, No. 1, 2009, pp. 198 – 217.

[38] Pointwise, "Pointwise V17," http://www.pointwise.com/pw/.

[39] Gill, P. E., Murray, W., and Saunders, M. A., "SNOPT: An SQP Algorithm for Large-Scale Constrained Optimization," *SIAM Review*, Vol. 47, No. 1, 2005, pp. 99–131.

[40] Hicken, J. E. and Zingg, D. W., "Aerodynamic Optimization Algorithm with Integrated Geometry Parameterization and Mesh Movement," *AIAA Journal*, Vol. 48, No. 2, 2017/04/17 2010, pp. 400–413.

[41] Biedron, R. T., Carlson, J.-R., Derlaga, J. M., Gnoffoo, P. A., Hammond, D. P., Jones, W. T., Kleb, B., Lee-Rausch, E. M., Nielsen, E. J., Park, M. A., Rumsey, C. L., Thomas, J. L., and Wood, W. A., "FUN3D Manual: 12.9," NASA TM-2016-219012, Langley Research Center, February 2016.

[42] Spalart, P. R. and Allmaras, S. R., "A One-Equation Turbulence Model for Aerodynamic Flows," *La Recherche Aerospatiale*, Vol. 1, No. 1, 1994, pp. 5–21.

[43] "K-Cluster," http://k-info.larc.nasa.gov/CCFresources_hardware.html, October 2013.

[44] Spalart, P. R., "Extensions of d'Alembert's paradox for elongated bodies," Tech. Rep. 2181, The Royal Society, 2015.

[45] Hartmann, R., "PADGE DG solver from Center for Computer Applications in AeroSpace Science and Engineering," http://www.dlr.de/as/en/desktopdefault.aspx/, 2006, Electronic Software.

[46] Milholen, W. E. and Owens, L. R., "On the Application of Contour Bumps for Transonic Drag Reduction (Invited)," Conference Proceedings 462, American Institute of Aeronautics and Astronautics, January 2005.

[47] Campbell, R., "Efficient viscous design of realistic aircraft configurations," AIAA 1998-2539, 29th AIAA, Fluid Dynamics Conference, Albuquerque, NM June 1998.

[48] Owens, L., "Private Correspondence," Discussion on TMA-0712 Airfoil.